Journal of
Materials Chemistry A

Materials for energy and sustainability
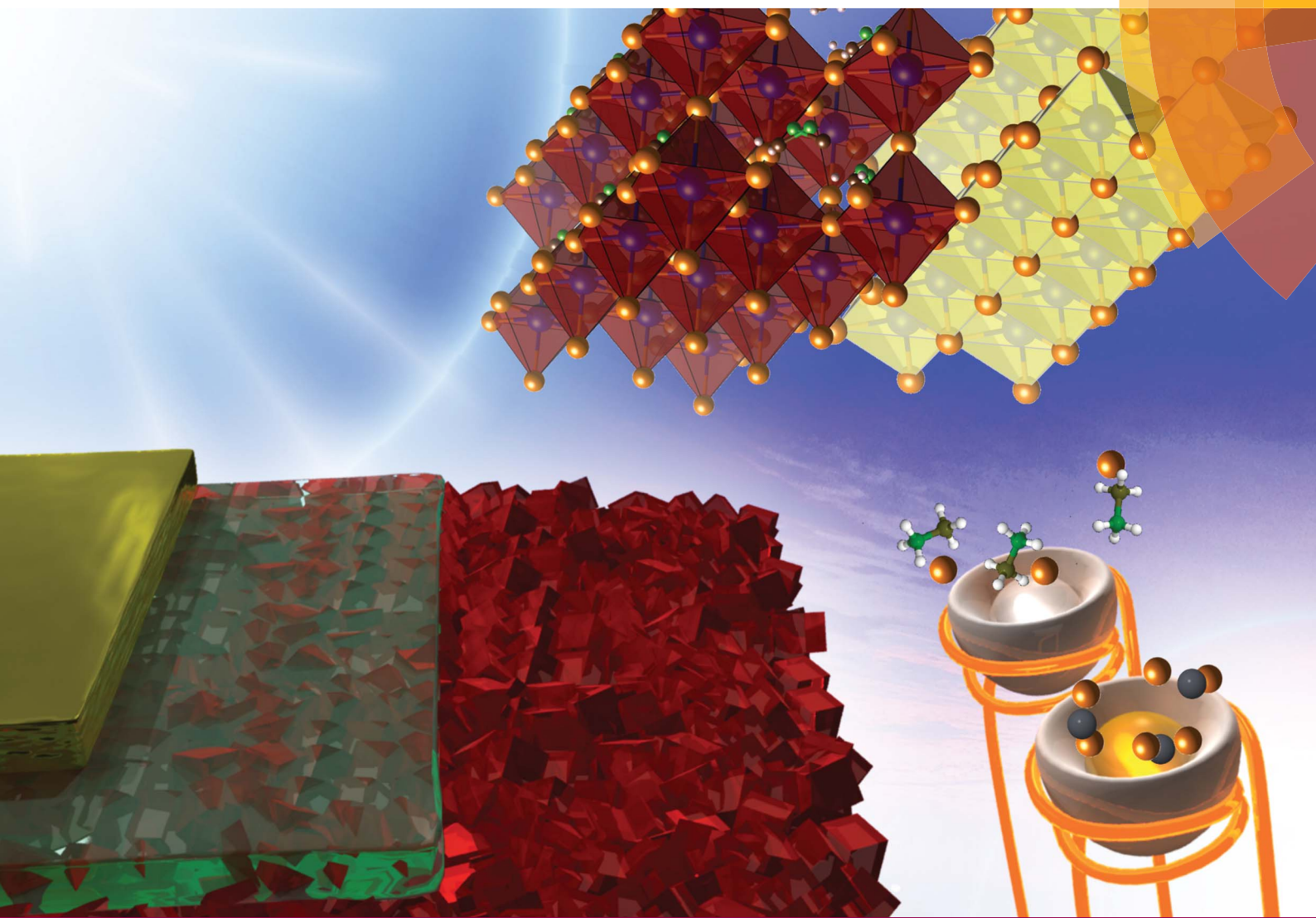
Emerging Investigators 2016: Novel design strategies for new functional materials

ROYAL SOCIETY
OF CHEMISTRY
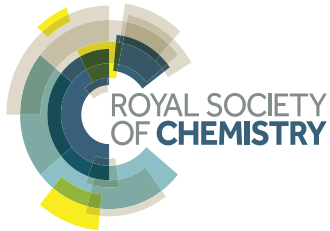
REVIEW ARTICLE
Yabing Qi *et al.*
Organometal halide perovskite thin films and solar cells by vapor
deposition

175 YEARS

REVIEW

CrossMark
click for updates

Organometal halide perovskite thin films and solar cells by vapor deposition

Luis K. Ono,† Matthew R. Leyden,† Shenghao Wang and Yabing Qi*

Organometal halide perovskites (OHPs) are currently under the spotlight as promising materials for new generation low-cost, high-efficiency solar cell technology. Within a few years of intensive research, the solar energy-to-electricity power conversion efficiency (PCE) based on OHP materials has rapidly increased to a level that is on par with that of even the best crystalline silicon solar cells. However, there is plenty of room for further improvements. In particular, the development of protocols to make such a technology applicable to industry is of paramount importance. Vapor based methods show particular potential in fabricating uniform semitransparent perovskite films across large areas. In this article, we review the recent progress of OHP thin-film fabrication based on vapor based deposition techniques. We discuss the instrumentation and specific features of each vapor-based method as well as its corresponding device performance. In the outlook, we outline the vapor deposition related topics that warrant further investigation.

1.   Introduction

Organometal halide perovskite (OHP) solar cells have emerged as the most promising candidate for the next generation high efficiency solar cell technology that is compatible with low-cost, low-temperature processing, flexible substrates, and large-area fabrication using *e.g.* ultrasonic spray-coating,[1] printing,[2] roll-to-roll,[3] and vapor deposition techniques.[4,5] Laboratory scale

cells with the highest power conversion efficiency (PCE) of ~20.1% were achieved in a short time span of four years,[6,7] which is only a few percent lower than the best single crystalline silicon solar cells.

The term perovskite refers to a category of materials that can be represented by the building block of ABX_3 and adopt a similar crystal structure to oxide perovskites such as calcium titanate $(CaTiO_3)$. A few review papers have been published on oxide and halide based perovskites with emphasis on solar cell application.[8–20] In the particular case of OHPs, the halide anions (X = I, Br, or Cl) and metal cations (B = Pb, Sn) form the BX_6 octahedral arrangement, Fig. 1a. The BX_6 octahedra extend to a three-dimensional network in which cations A can be stabilized within

Energy Materials and Surface Sciences Unit (EMSS), Okinawa Institute of Science and Technology Graduate University (OIST), 1919-1 Tancha, Onna-son, Okinawa, 904-0495, Japan. E-mail: Yabing.Qi@OIST.jp

† These authors contributed equally.

Luis K. Ono is a staff scientist in Prof. Yabing Qi's Unit (Energy Materials and Surface Sciences Unit) at Okinawa Institute of Science and Technology Graduate University in Japan. He obtained his B.S. in Physics/Microelectronics in 2000 from the University of São Paulo, Brazil. Later he joined the Department of Nuclear Engineering in Kyoto University, Japan, and the University of Central Florida, USA, where he obtained his M.S. in 2003 and Ph.D. in 2009, respectively. His current research focuses on the fundamental understanding of perovskite solar cells.

Matthew Leyden received his Bachelor of Science in physics from Cal Poly San Luis Obispo in 2005, and then went on to receive his Ph.D. in physics from Oregon State University in 2011. He currently works as a post-doctoral scholar in Prof. Yabing Qi's Unit at Okinawa Institute of Science and Technology Graduate University researching perovskite synthesis by chemical vapor deposition.

This journal is © The Royal Society of Chemistry 2016

J. Mater. Chem. A, 2016, **4**, 6693–6713 | **6693**

the space formed by the eight adjacent octahedra (Fig. 1).[21] The larger cation A (A being larger than B) can be Cs^+,[22] methylammonium ($CH_3NH_3^+$, MA^+), ethylammonium ($CH_3CH_2NH_3^+$, EA^+),[15] formamidinium ($NH_2CH=NH_2^+$, FA^+),[23] or mixed CH_3NH_3 and 5-aminovaleric acid (5-AVA) cations [(5-AVA)$_x$(CH_3NH_3)$_{1-x}$].[2] The crystallographic stability and probable structure are estimated by considering the Goldschmidt tolerance factor and the octahedral factor.[9,15,16,24] Nevertheless, the determination of chemical and thermal stability of the resultant perovskite structure requires more detailed analysis.[10] CH_3-NH_3PbI_3, the most commonly employed material in OHP solar cells, was reported to have a high absorption coefficient (direct bandgap of ~1.55 eV) and high mobilities for electrons (7.5 cm^2 V^{-1} s^{-1}) and holes (12.5–66 cm^2 V^{-1} s^{-1}), i.e. ambipolar nature, resulting in long carrier diffusion lengths (100 nm to 1 μm).[25] Although the amount and role of incorporated Cl are still under debate,[26] mixed methylammonium-lead halide $CH_3NH_3PbI_{3-x}$-Cl$_x$ is another type of halide perovskite reported with an even higher charge-carrier mobility (~33 cm^2 V^{-1} s^{-1}), resulting in carrier diffusion lengths of up to 3 μm.[27] Theoretical studies have shown that most point defects in OHP form shallow defect states.[28–32] In addition, grain boundaries were shown that they do not generate gap states, which makes the electronic property behavior of polycrystalline halide perovskite similar to that of a thin-film single crystal.[28,29,33] In a recent work by deQuilettes et al.,[34] the existence of large spatial variations in photoluminescence (PL) intensity and carrier recombination lifetimes were probed using a confocal PL microscope. In particular, higher contrasts were observed at the grain boundaries in comparison to the bulk of the material within the individual grains of $CH_3NH_3PbI_{3-x}$Cl$_x$ perovskites.[34] Differences in PL intensities were attributed to the variations in radiative and nonradiative recombination dynamics.[34] The question whether the perovskite solar cell system is excitonic, similar to an organic solar cell, which requires a heterojunction interface to separate electron–hole pairs, or instead photoexcitations spontaneously dissociate into free carriers in the bulk, similar to inorganic solar cells, has not been completely settled.[35–39] On the other hand, a number of studies suggest that exciton binding energies (BEs) in perovskites are in the range of ~2–50 meV,[35] and ultrafast interfacial charge-transfer dynamics take place;[36] collectively, the majority of these observations imply that perovskite solar cells are predominantly non-excitonic similar to inorganic solar cells showing relatively low exciton BEs, e.g., Si (15.0 meV), GaAs (4.2 meV), and CdTe, (10.5 meV).[37]

In the 1990s, Mitzi and co-workers studied OHPs and discovered desirable physico-chemical properties of these materials mainly for electronic applications.[40–42] Almost in parallel, Grätzel and co-workers developed a new class of photovoltaic technology, dye-sensitized solar cells (DSSCs or Grätzel cell) and solid-state DSSCs (ssDSSCs) shown in Fig. 2.[14,43,44] Miyasaka and co-workers were the first to apply perovskites in DSSCs in 2009.[45] The dye was replaced by methylammonium lead triiodide/tribromide ($CH_3NH_3PbI_3$ and $CH_3NH_3PbBr_3$) perovskites in DSSC configuration[13,14] obtaining a PCE of ~3.8% and ~3.1%, respectively, using the iodine/triiodide redox liquid electrolyte as the hole-transport material. Due to the high instabilities of the perovskite materials in the electrolytes, ruthenium-based dyes were still the preferable choice. In 2012, Park and co-workers fabricated all solid-state perovskite ($CH_3NH_3PbI_3$) solar cells and achieved a PCE of ~9.7% and much better durability.[46] The key advance was made possible by replacing the liquid electrolyte with a solid hole transporting layer (HTL) material, Fig. 2.[46] Since then, a myriad of reports have been published exploring the different perovskite materials, various device architectures, and fabrication methods.[14,47–50] Both the dye and $CH_3NH_3PbI_3$ assume the function of a sensitizer in which light absorption induces subsequent electron injection into the conduction band of the mesoporous TiO$_2$ scaffold (electron transport layer, ETL) accompanied by hole injection from the oxidized sensitizer to the highest-occupied molecular orbital (HOMO) of the HTL.

Shenghao Wang received his Master's degree in Condensed Matter Physics from Sichuan University, China and Doctor's degree in Applied Physics from University of Tsukuba, Japan, in 2010 and 2013, respectively. After that, he worked as a post-doctoral researcher in Akimoto Laboratory in University of Tsukuba. Currently he is a post-doctoral scholar in Prof. Yabing Qi's Unit (Energy Materials and Surface Sciences Unit) at Okinawa Institute of Science and Technology Graduate University (OIST). His research interests include surface and interface sciences, photoemission spectroscopy techniques, organic solar cells, and organic–inorganic hybrid perovskite solar cells.

Yabing Qi is currently an Assistant Professor and Head of Energy Materials and Surface Sciences Unit (EMSS) in Okinawa Institute of Science and Technology Graduate University (OIST). Dr Qi received his B.S., M.Phil., and Ph.D. degrees from Nanjing University, Hong Kong University of Science and Technology, and University of California Berkeley, respectively. His research interests include perovskite solar cells, organic electronics, surface sciences, energy materials and devices. Dr Qi has co-authored ~50 peer-refereed papers and has delivered 70+ invited and contributed research presentations at international conferences, technical meetings and universities.

6694 | J. Mater. Chem. A, 2016, 4, 6693–6713

This journal is © The Royal Society of Chemistry 2016
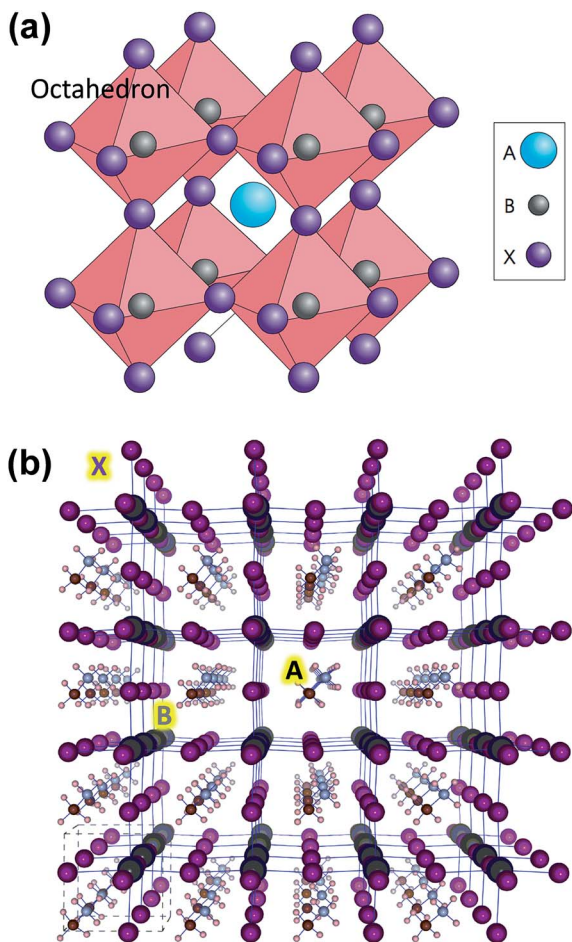
Fig. 1 (a) Ideal cubic perovskite structure with B metals assembled around X anions to form BX_6 octahedron. A cation fills the space formed by the eight adjacent octahedra and balances the charge of the whole network. Reprinted with permission from Macmillian Publishers Ltd: Nature Photonics (ref. 15), copyright (2014). (b) Optimized structure for (pseudo)-cubic $CH_3NH_3PbI_3$ with $4 \times 4 \times 4$ supercell. Color coding: large dark gray: lead; purple: iodine; brown: carbon; small light gray: nitrogen; white: hydrogen atoms. Reprinted with permission from ref. 21. Copyright (2013) American Chemical Society.

Further charge transport of electron and hole through the external circuit completes the photovoltaic operation.[8] The use of TiO_2 and HTL as selective contacts ensures that photoexcited charge carriers (electrons and holes) are transported in opposite directions. In a separate experiment, Lee *et al.*[47] showed that a mesoporous (mp-) scaffold made of Al_2O_3 instead of TiO_2 generated a similar PCE even though Al_2O_3 is an insulating material. This paradigm has been rationalized by suggesting that perovskite itself is a good electron conductor; if so, no mp-TiO_2 scaffold is necessary at all. This led to a much simpler planar-type device architecture, Fig. 2, and first confirmed by Liu *et al.*,[4] who showed efficient (PCE ~ 15.4%) CH_3NH_3-$PbI_{3-x}Cl_x$ based perovskite solar cells without employing any mesoporous metal oxide layer. Etgar *et al.*[51] had demonstrated that $CH_3NH_3PbI_3$ could also act as an efficient hole conductor, which could even eliminate the need for employing the additional HTL layer. However, generally both electron and hole

selective contacts contribute to the enhancement of the cell fill factor (FF). In particular, the hole selective contact tends to enhance the open-circuit voltage (V_{oc}) by minimizing interfacial charge recombination processes, *i.e.* the HTL performs both functions of blocking electrons as well as transporting holes efficiently.[52]

The film morphology, thickness, stoichiometry, crystallinity as well as material purity have significant impact on the overall solar cell performance. A variety of solution- and vapor-based OHP deposition techniques have been reported including one-step spin-coating,[53–57] two-step deposition techniques,[41,58–60] solvent–solvent extraction,[61] vapor-assisted solution processes,[62–69] dual-source vacuum deposition,[4,5,70–77] hybrid deposition,[78–81] hybrid chemical vapor deposition,[82–87] sequential vapor deposition,[88–92] flash evaporation,[93] *etc.* One-step spin-coating is one of the widely used methods because of its simplicity and low-cost. However, the films prepared by this method often have a poor morphology (incomplete coverage) especially in the case of planar architecture, which results in decreased solar cell performance.[54,94–96] In the two-step process,[41,58,59] a layer of metal halide is deposited by spin-coating followed by dipping the film into the organic salt solution and perovskite formed by a chemical reaction. However, due to the high reaction rates of perovskite formation, it is challenging to optimize the processing conditions with sufficient reproducibility.[97] Despite the fact that laboratory record efficiencies have been obtained by solution processing,[7,50,98] it is observed that the reaction kinetics need to be rigorously controlled to maintain consistent device performance and minimize batch-to-batch variations.[99] Yang and co-workers introduced a CH_3NH_3I vapor-based approach for the deposition of a perovskite layer called vapor-assisted solution process (VASP).[62,63,65] In their process, PbI_2 films were annealed in MAI vapor at 150 °C in an N_2 environment for 2 h, Fig. 3a. Perovskite films exhibited high crystallinity, uniform surface coverage and large grain sizes up to 1 micrometer, Fig. 3b–d. The high quality films of $CH_3NH_3PbI_3$ enabled enhanced solar cell parameters of short-circuit current (J_{sc}), V_{oc}, FF, and PCE: 19.8 mA cm^{-2}, 0.924 V, 0.663, 12.1%, respectively, in a planar architecture, Fig. 3e.[62,63] The surface roughness of the films was measured by atomic force microscopy (AFM) (5×5 μm^2, Fig. 3f) and calculated to be 23.2 nm. In a recent publication, the authors state that it is still unclear why the efficiency of perovskite solar cells based on VASP is slightly lower than that of devices derived from an optimized solution process.[65] In this review, we focus on the different vapor-based methods to deposit perovskite films, which in many cases show properties different from their counterparts prepared by solution-based methods.

2. Vapor deposition by dual-source

2.1. Vapor deposition system description

Vapor deposition techniques are widely used in the semiconductor industry aiming at large scale production in optoelectronic applications. The viability of OHP material synthesis by physical vapor deposition techniques has also been demonstrated.[4,5,70–74,100] Such techniques offer unique advantages such as (1) it is feasible to fabricate films with high-
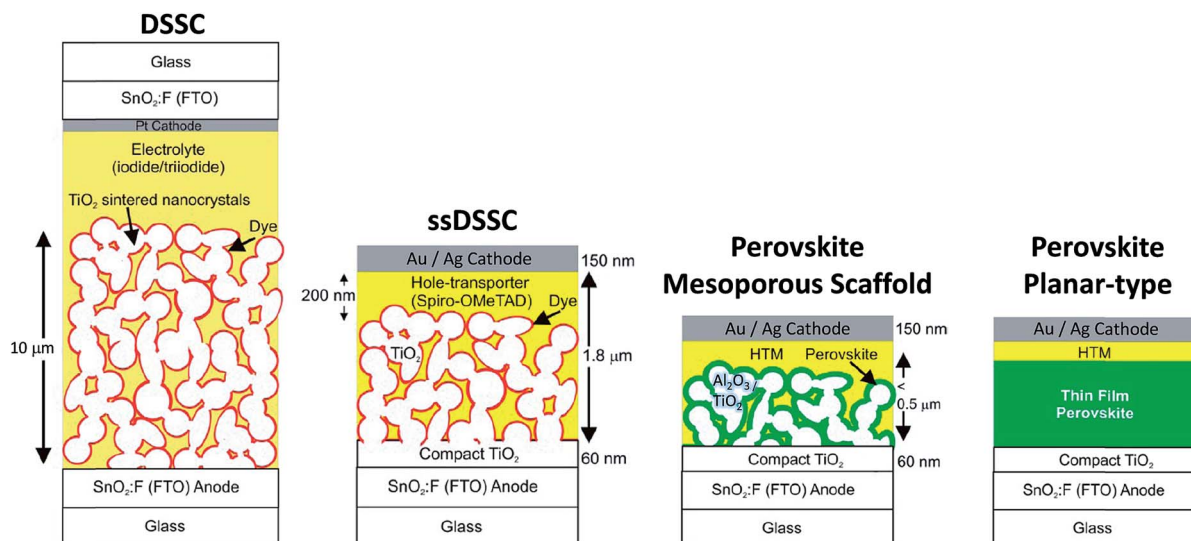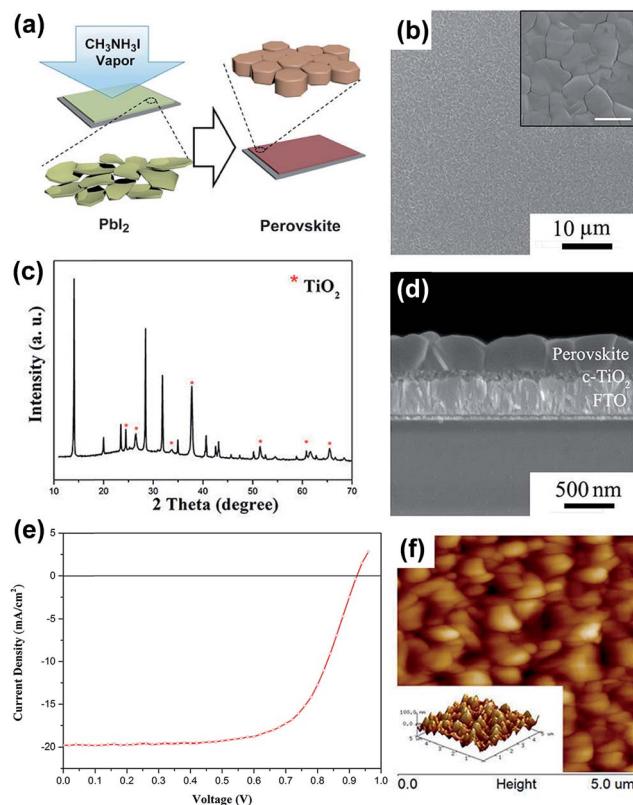
Fig. 2 Evolution of the solar cell technology starting from the electrolyte-based mesoscopic DSSC and solid state (ss) DSSC where the electrolyte is replaced with an organic p-type hole conductor. Structural evolution of perovskite-based solar cells evolved from (i) sensitized solar cell with nanodot perovskite; (ii) mesoporous (scaffold) structured solar cell with a thin and continuous layer of perovskite; (iii) perovskite-infiltrated solar cell with a capping layer of perovskite; (iv) thin film planar heterojunction perovskite solar cell. Adapted with permission from ref. 14. Copyright (2013) American Chemical Society.

purity as the films are formed by sublimating the powder precursors after extensive outgassing under a vacuum environment; (2) in general, the initial nominal stoichiometry of precursors (e.g., CH_3NH_3I and $PbCl_2$) can be well controlled in both solution and vacuum evaporation methods. On the other hand, it is necessary to take into account the solubility of precursors in determining the composition of the films that are prepared by solution methods. For example, it is difficult to dissolve $PbCl_2$ in N,N-dimethylformamide (DMF) when the $CH_3NH_3I : PbCl_2$ molar ratio is lower than 3 : 1.[47] (3) The commonly used solvents, in the solution process, can get intercalated in perovskite films. DMF, H_2O, and dimethylsulfoxide (DMSO) were observed to form stable intermediate complexes of $CH_3NH_3PbI_3 \cdot DMF$,[101] $CH_3NH_3PbI_3 \cdot H_2O$,[102] and $CH_3NH_3PbI_3 \cdot DMSO$,[103] respectively, likely to affect the perovskite film stability. (4) Vapor deposition techniques are suitable for the preparation of multilayered structures of thin films, while it is challenging for solution processing. (5) With proper optimization, perovskite films can be deposited by vapor deposition on a variety of substrates. The wettability issues in solution processing often lead to non-uniform coating and pin-hole formation.

In 1997, Era et al.[104] reported for the first time the dual-source vapor deposition method to form two-dimensional layered hybrid lead iodide intercalated with an organic ammonium layer. The synthesis of $(RNH_3)_2PbI_4$ layered perovskite was performed under a pressure of $\sim 10^{-6}$ Torr sublimating PbI_2 and organic ammonium iodide RNH_3I (2-phenylethylammonium iodide $C_6H_5C_2H_4NH_3I$ was used as RNH_3I). The synthesis of $KPbI_3$ under vacuum from the PbI_2 and KI precursor sources was reported by Salau.[105] $KPbI_3$ has been suggested as a potential candidate for solar cell applications because of its high thermal stability (220 °C).[105]

In 2013, Liu et al.[4] reported the synthesis of three-dimensional $CH_3NH_3PbI_{3-x}Cl_x$ by using the dual-source vapor deposition technique with $PbCl_2$ and CH_3NH_3I as precursors leading to high efficiency photovoltaic devices (PCE $\sim 15.4\%$, Table 1). Similarly, Malinkiewicz et al. deposited a pure $CH_3NH_3PbI_3$ perovskite by using PbI_2 and CH_3NH_3I sources showing uniform film formation with a root mean square (RMS) roughness of 5 nm measured by AFM.[5] In addition, the films showed uniform grainy structures with an average grain size of 150 nm.[71] The schematic illustration of the dual-source vacuum deposition process is shown in Fig. 4.[71,75] PbX_2 (X = I, Cl) and CH_3NH_3I precursor materials contained in crucibles are heated (co-evaporation) to their corresponding sublimation temperatures. $CH_3NH_3PbI_{3-x}Cl_x$ and $CH_3NH_3PbI_3$ perovskites layers are formed on the substrate that is fixed at a distance of ~ 20 cm above the crucibles.[5] Typical base pressures of 10^{-5} to 10^{-6} Torr are reached after loading the precursor materials.[4,5] The stoichiometry (chemical composition) and film thickness are monitored with the aid of piezo-electric sensors[4,5] mounted inside the vacuum chamber (or a quartz crystal microbalance, QCM). Because perovskites are formed by the co-evaporation process, it requires the initial calibration as precise as possible for the thicknesses of individual evaporated PbX_2 and CH_3NH_3I films. Material density (ρ), acoustic impedance (or Z-ratio), and geometric (or tooling factor) are parameters that need to be determined for the calibration of evaporation rate of the material being sublimated. Often it is difficult to find those parameters especially for organic compounds. For example, Liu et al. assumed the density and Z-ratio of CH_3NH_3I to be 1 g cm^{-3} and 1, respectively, because its precise density is unknown.[4] The density for CH_3NH_3Cl of 1.1 g cm^{-3} was previously reported.[4] More recently, the density value of 2.224 g cm^{-3} for CH_3NH_3I has been reported.[80] In addition, the tetragonal $CH_3NH_3PbI_3$ perovskite phase was calculated to have a density of 4.149 g cm^{-3}.[80]

Fig. 3 (a) Schematic illustration of the vapor-assisted solution process (VASP). Perovskite film on the FTO/c-TiO₂ substrate, obtained by reacting PbI₂ film and CH₃NH₃I vapor at 150 °C for 2 h in an N₂ atmosphere; (b) top-view SEM image (inset image with higher resolution, scale bar 1 μm); (c) XRD pattern; (d) cross-sectional SEM image; (e) $J–V$ characteristics of CH₃NH₃PbI₃ based solar cell generating efficiencies of 12.1% under AM1.5G illumination. Spiro-MeOTAD and Ag were used as the HTL and top electrode, respectively; (f) tapping-mode AFM height images (5 × 5 μm²) (inset: the corresponding 3D topographic image). The corresponding surface roughness of 23.2 nm was reported. Reprinted with permission from ref. 62. Copyright (2013) American Chemical Society.

The densities of $PbCl_2$ and PbI_2 can be found in the literature with typical values of 5.85 g cm⁻³ and 6.16 g cm⁻³, respectively. As the source-to-substrate distance generally differs from the source-to-QCM distance, it is often a common practice to perform some initial tests to determine the tooling factor. A certain amount of material is deposited on a flat substrate recording the nominal thickness measured by the QCM with a preset tooling factor value. This nominal thickness value is then compared to the thickness value determined using another technique (*e.g.*, AFM or surface profilometry). The linear relationship provides the new tooling factor of the evaporation system. As it will be discussed in more detail in the next section (3. Hybrid deposition method), the calibration procedure for the CH₃NH₃I was reported to be difficult due to the formation of a non-uniform layer dominated by the Volmer–Weber or Stranski–Krastanov growth mode and the volatile nature of the organic film.[5,71,78,79] Alternatively Malinkiewicz *et al.*[5,71] kept the evaporation temperature for the CH₃NH₃I crucible constant (at 70 °C) and varied the CH₃NH₃I : PbI₂ ratio by changing only the

evaporation temperature of the PbI₂ crucible (250–260 °C). The optimum conditions were determined by analyzing the evaporated perovskite films by grazing incident X-ray diffraction (GIXRD). Once the optimum PbI₂ crucible temperature (250 °C) for generating the stoichiometric perovskite is determined, perovskite films with similar properties can be prepared reproducibly indicating the robustness of the protocol.[5,71]

The substrate holder is maintained at near room-temperature during perovskite deposition for the processes described above.[4,5,71] Because of low-temperature processing, it is highlighted that the technique is of particular interest for the deposition of perovskite films onto flexible substrates. Liu *et al.*[4] provide side-by-side comparison on the morphology of the CH₃NH₃PbI₃₋ₓClₓ perovskite films prepared by the solution and dual-source vacuum evaporated films. For example, the top- and side-views of scanning electron microscopy (SEM) highlight that vacuum-deposited films show full coverage and are extremely uniform with crystalline features on the size scale of hundreds of nanometers, Fig. 5a and b. Large-area cross-sectional SEM images, Fig. 5c and d, reveal that solution-processed films exhibit large variations in film thickness (50 to 410 nm) over the sample area, whilst vacuum-evaporated films have a constant film thickness of ∼330 nm. X-ray diffraction (XRD) patterns for both solution- and vacuum-processed show the main diffraction peak positions to be identical indicating that both techniques generate similar mixed-halide perovskite, Fig. 5e. The observed diffraction peaks at 14.12°, 28.44°, and 43.23° are assigned to the (110), (220), and (330) planes of the orthorhombic crystal structure.[47] The small peak at 12.65° is assigned to the (110) diffraction peak of the remaining PbI₂ compound. The best solar cell device based on the planar heterojunction architecture of FTO/c.l.-TiO₂/CH₃NH₃PbI₃₋ₓClₓ/spiro-MeOTAD/ Ag generates solar cell parameters of J_{sc}, V_{oc}, FF, and PCE: 21.5 mA cm⁻², 1.07 V, 0.67, 15.4%, respectively, Fig. 5f.

More recently, Lin *et al.*[37] reported the use of vacuum-processed CH₃NH₃PbI₃-perovskite planar structures with optimized ultrathin n- and p-type organic interlayers of PCBM and PCPDTBT, respectively, which serve to modify the electrode work functions. Enhanced solar cell parameters were obtained: J_{sc} = 21.9 mA cm⁻², V_{oc} = 1.05 V, FF = 0.72, and PCE = 16.5%. The complete devices (ITO/PEDOT:PSS/PCPDTBT/CH₃NH₃PbI₃/ PCBM/LiF/Ag) had an active area of 0.2 cm².

2.2. Large-area solar cell

The first attempt for the fabrication of a larger-area solar cell (0.95 cm²) was reported by Malinkiewicz *et al.* in an inverted device architecture (ITO/PEDOT:PSS/polyTPD/CH₃NH₃PbI₃/ PCBM/3TPYMB/Au), Fig. 6. In most reports the active area sizes of the cells are smaller than 0.1 cm², Table 1. Despite the general trend of lower FF as the active area increased, the authors observed that the high V_{oc} was maintained and attributed to negligible surface and sub-bandgap trap states in vacuum-deposited perovskite films.[5] The industrial-scale manufacturing of perovskite solar cells urgently calls for methods that are suitable to coat high-quality perovskite films over a large area (*e.g.* 1 cm² or larger).[15]

This journal is © The Royal Society of Chemistry 2016

J. Mater. Chem. A, 2016, **4**, 6693–6713 | **6697**

Table 1 Summary of perovskite solar cells in a planar configuration with perovskite thin-films synthesized by the different vapor-based techniques. Perovskite thicknesses, electrode active areas, solar cell parameters of short-circuit current (J_{sc}), open-circuit voltage (V_{oc}), fill factor (FF), and power conversion efficiency (PCE), and normalized PCE by film thickness are indicated

Solar cell architecture[a]	Perovskite thickness (nm)	Electrode active area (cm^2)	J_{sc} (mA cm^{-2})	V_{oc} (V)	FF	PCE (%)	Norm. PCE/thickness (×%/100 nm)	Ref.
FTO/c.l.-TiO$_2$/CH$_3$NH$_3$PbI$_{3-x}$Cl$_x$/spiro/Ag (co-evaporation)	330	0.076	21.5	1.07	0.68	15.4	4.7	4
ITO/PEDOT:PSS/polyTPD/CH$_3$NH$_3$PbI$_3$/ PCBM/Au (co-evaporation)	285	0.09	16.12	1.05	0.67–0.68	12.04	4.2	5
	285	0.98	14.76	1.05	0.52	8.27	2.9	
ITO/PEDOT:PSS/polyTPD/CH$_3$NH$_3$PbI$_3$/ PCBM/Au (co-evaporation)	285	0.06	18.8	1.07	0.63	12.7	4.5	70
ITO/PEDOT:PSS/polyTPD/CH$_3$NH$_3$PbI$_3$/ PCBM/3TPYMB/Au (co-evaporation)	285	0.065	18.2	1.09	0.75	14.8	5.2	71
	285	0.95	17.9	1.07	0.57	10.9	3.8	
ITO/PEDOT:PSS/PCDTBT/CH$_3$NH$_3$PbI$_3$/ PC$_{60}$BM/LiF/Ag (co-evaporation)	370	0.2	21.9	1.05	0.72	16.5	4.5	37
FTO/NiO/CH$_3$NH$_3$PbI$_{3-x}$Cl$_x$/PCBM/Ag (co-evaporation)	250	0.07	14.2	0.786	0.65	7.26	2.9	72
FTO/CuSCN/CH$_3$NH$_3$PbI$_{3-x}$Cl$_x$/PCBM/Ag (co-evaporation)	500	0.07	∼8.8	0.677	—[b]	3.8	0.8	72
ITO/F6-TCNNQ/spiro-MeO-TPD/ CH$_3$NH$_3$PbI$_{3-x}$Cl$_x$/C$_{60}$/Ag (co-evaporation)	390	0.064	16.0	1.03	0.66	10.9	2.8	74
ITO/MoO$_3$/NPB/CH$_3$NH$_3$PbI$_3$/C$_{60}$/BCP/Al (co-evaporation)	320	0.04	18.1	1.12	0.68	13.7	4.2	73
ITO/CH$_3$NH$_3$PbI$_{3-x}$Cl$_x$/C$_{60}$/Bphen/Al (co-evaporation)	150	0.1	12.5	0.82	0.60	6.1	4.1	76
FTO/PEDOT:PSS/CH$_3$NH$_3$PbI$_{3-x}$Cl$_x$/ PCBM/Ag (co-evaporation)	400	0.12	17.3	0.97	0.63	10.5	2.6	77
FTO/c.l.-TiO$_2$/CH$_3$NH$_3$PbI$_{3-x}$Cl$_x$/spiro/Ag (hybrid deposition)	50	0.05	10.5	1.06	0.566	6.3	12.6	78
	135	0.05	17.0	1.09	0.535	9.9	7.3	
FTO/c.l.-TiO$_2$/CH$_3$NH$_3$PbI$_3$/spiro/Au (hybrid deposition)	170	0.05	19.92	1.098	0.524	11.48	6.8	79
FTO/c.l.-TiO$_2$/CH$_3$NH$_3$PbI$_3$/spiro/Au (hybrid deposition)	270–300	0.16	∼18	>1.1	>0.7	>12	>4.4	80
FTO/C$_{60}$/CH$_3$NH$_3$PbI$_3$/spiro/Au (hybrid deposition)	320	0.08	18.9	1.10	0.754	15.7	4.9	81
FTO/C$_{70}$/CH$_3$NH$_3$PbI$_3$/spiro/Au (hybrid deposition)	320	0.08	18.6	1.03	0.777	14.9	4.7	
FTO/c.l.-TiO$_2$/CH$_3$NH$_3$PbI$_{3-x}$Cl$_x$/spiro/Au (hybrid CVD)	296	0.07–0.1	19.1	0.92	0.62	10.8	3.6	82
FTO/c.l.-TiO$_2$/HC(NH$_2$)$_2$PbI$_{3-x}$Cl$_x$/spiro/ Au (hybrid CVD)	324	0.04–0.169	20.9	1.03	0.66	14.2	4.4	83
	324	1	18.4	0.97	0.43	7.7	2.4	
FTO/c.l.-TiO$_2$/CH$_3$NH$_3$PbI$_3$/spiro/Ag (low-pressure CVD)	—[b]	0.12	21.7	0.91	0.65	12.73	—	85
FTO/c.l.-TiO$_2$/CH$_3$NH$_3$PbI$_3$/spiro/Ag or Au (*in situ* tubular CVD)	320	0.12	21.0	0.952	0.61	12.2	3.8	84
ITO/PEDOT:PSS/CH$_3$NH$_3$PbI$_{3-x}$Cl$_x$/C$_{60}$/ Bphen/Ca/Ag (sequential deposition)	430	0.05	20.9	1.02	0.722	15.4	3.6	88
ITO/CH$_3$NH$_3$PbI$_3$/C$_{60}$/Ag (sequential deposition)	∼350	0.09	13.6	0.8	0.5	5.4	1.5	89
FTO/c.l.-TiO$_2$/CH$_3$NH$_3$PbI$_3$/spiro/MoO$_3$/ Al (sequential deposition)	473	0.09	21.8	0.96	0.6	12.5	2.6	90
FTO/c.l.-TiO$_2$/CH$_3$NH$_3$PbI$_3$/P3HT/Au (sequential deposition)	∼400	0.104	21.76	0.96	0.653	13.7	3.4	91
FTO/c.l.-TiO$_2$/CH$_3$NH$_3$PbI$_{3-x}$Cl$_x$/spiro/Au (sequential deposition)	412	0.071	22.27	1.00	0.72	16.03	3.9	92
		0.49	20.91	0.98	0.69	14.14	3.4	
		1	20.77	0.98	0.68	13.84	3.4	
ITO/PEDOT:PSS/CH$_3$NH$_3$PbI$_3$/polyTPD/ PCBM/Ba/Ag (flash evaporation)	200	—[b]	18	1.067	0.68	12.2	6.1	93

^{a} Abbreviations: FTO = fluorine doped tin oxide; c.l.-TiO$_2$ = compact layered TiO$_2$; spiro = 2,7′–7,7′-tetrakis-(*N,N*-di-*p*-methoxyphenylamine)-9,9′-spirobifluorene; ITO = indium tin oxide; PEDOT-PSS = poly(3,4-ethylenedioxy-thiophene):poly(styrene sulfonate); polyTPD = poly(*N,N*′-bis(4-butylphenyl)-*N,N*′-bis(phenyl)benzidine); PCBM = (6,6)-phenyl C$_{61}$-butyric acid methyl ester; Bphen = bathophenanthroline; NPB = *N,N*′-di(1-naphthyl)-*N,N*′-diphenyl-(1,1′-biphenyl)-4,4′-diamine; BCP = bathocuproine; 3TPYMB = tris(2,4,6-trimethyl-3-(pyridine-3-yl)phenyl)borane; F6-TCNNQ = 2,2′-(perfluoronaphtalene-2,6-diylidine)dimalononitrile; spiro-MeO-TPD = 2,7-bis[*N,N*-bis(4-methoxy-phenyl)amino]-9,9-spirobifluorene; PCDTBT = poly(*N*-9′-heptadecanyl-1,2,7-carbazole-*alt*-5,5-(4′,7′-di(thien-2-yl)-2′1′,3′-benzothia-diazole). ^{b} Not provided.

6698 | *J. Mater. Chem. A*, 2016, **4**, 6693–6713

This journal is © The Royal Society of Chemistry 2016
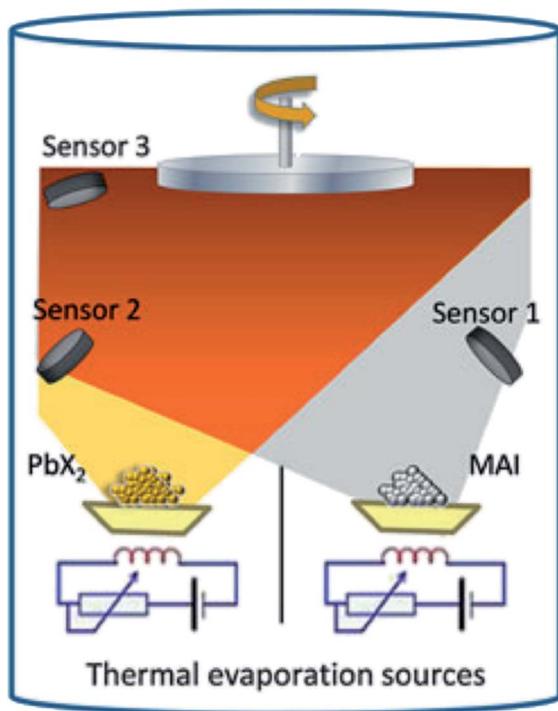
Fig. 4 Illustration of the dual-source vacuum deposition instrument. The PbX_2 (X = I, Cl) and CH_3NH_3I (MAI) precursors are thermally evaporated in vacuum. The deposition rate and thickness are monitored using quartz microbalances. Reproduced with permission from ref. 75.

2.3. Vacuum deposition of HTL

The top selective contacts (either ETL or HTL) in perovskite-based solar cells can be influenced by the doping and environmental conditions (air, humidity, temperature, and light-soaking) in which the cell is being operated.[106–109] Efforts have been made to find ETL/HTL materials that are less influenced by environmental conditions, which is expected to help minimize batch-to-batch variations.[70,72–74] For example, Momblona et al.[70] fabricated the inverted structure solar cell (ITO/
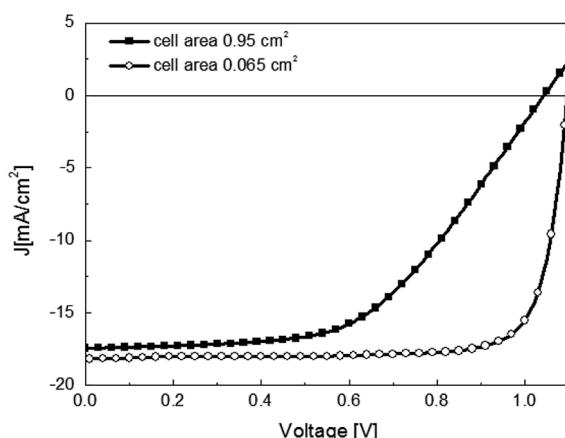
Fig. 6 $J–V$ curves for the optimized $CH_3NH_3PbI_3$ perovskite layer with a small (A = 0.065 cm^2) and larger (A = 0.95 cm^2) electrode size. The solar cell in planar heterojunction architecture is composed by ITO/PEDOT:PSS/PolyTPD/$CH_3NH_3PbI_3$/PCBM/3TPYMB/Au. Reproduced with permission from ref. 71.

Fig. 5 (a) SEM top-view of vacuum-deposited $CH_3NH_3PbI_{3-x}Cl_x$ perovskite film. (b) Cross-sectional SEM image under high magnification of the complete cell fabricated from vacuum-deposited perovskite film. (c and d) Cross-sectional SEM images under lower magnification comparing the (c) vacuum- and (d) solution-processed perovskite films. (e) XRD spectra of vacuum- and solution-processed perovskite films. $J–V$ curves of the best performing vacuum- and solution-processed planar heterojunction perovskite solar cells measured under AM1.5 (101 mW cm^{-2}) irradiance and in the dark. Reprinted with permission from Macmillan Publishers Ltd: Nature (ref. 4), copyright (2013).

PEDOT:PSS/polyTPD/$CH_3NH_3PbI_3$/PCBM/Au) by varying the perovskite layer thicknesses from 200 nm to 900 nm. J_{sc} was observed to increase as the perovskite layer thickness increased, and the rate of J_{sc} increase was faster at the beginning up to 300 nm and slower for devices with thicker active layers. The devices with thicker perovskite layers were observed to have lower FF reducing the overall PCE. The cell with a 900 nm perovskite film thickness was still able to generate respectable solar parameters of J_{sc}, V_{oc}, FF, and PCE: 19.8 mA cm^{-2}, 0.92 V, 0.4, 7.2%, respectively. Interestingly, the authors observed that replacing the pristine polyTPD with a slightly p-doped version of polyTPD (0.05% oxidized) in the cell with a 900 nm perovskite layer led to the significant improvement of the FF and PCE (J_{sc} = 19.5 mA cm^{-2}, V_{oc} = 0.94 V, FF = 0.65, and PCE = 12%). This work showed that with an appropriate HTL, solar cell PCEs had only a weak dependence on the perovskite film thickness. In addition, it demonstrated the properties of long diffusion lengths for electrons and holes in vacuum-processed perovskite films.

Perovskite solar cells using inorganic hole conductors (such as NiO, CuI, and CuSCN) as HTLs have received attention because of their better stability than HTLs using spiro-MeO-TAD.[72,110,111] Subbiah et al.[72] reported the initial attempts of vacuum-deposited $CH_3NH_3PbI_{3-x}Cl_x$ perovskite employing NiO and CuSCN, Table 1. Although the reported PCEs were much lower compared to those employing organic HTLs, it represents a promising step toward stability.

Schulz et al.[112] identified that V_{oc} losses of up to 0.4 eV could arise from an ionization energy (IE) mismatch between the spiro-MeOTAD HTL (IE = 5.0 eV) and $CH_3NH_3PbI_{3-x}Cl_x$ perovskite (IE = 5.4 eV). Polander et al.[74] reported fully vacuum-processed planar heterojunction $CH_3NH_3PbI_{3-x}Cl_x$ perovskite solar cells using various p-doped HTLs with different IE values ranging from 5.0 eV to 5.6 eV and C_{60} as the ETL. The authors studied the influences of the energy level mismatch between the valence band maximum (VBM) of $CH_3NH_3PbI_{3-x}Cl_x$ (IE = 5.4 eV) perovskite and the different HTLs on the solar cell performance. It has been shown that the IE of the HTL correlates with the V_{oc} of solar cell devices. Devices employing HTLs with IEs of up to 5.3 eV yielded a high V_{oc} and PCE. In contrast, with IEs beyond 5.3 eV, a substantial decrease in both J_{sc} and V_{oc} was observed, which was attributed to the absence of driving force for hole extraction. Optimized solar cells employing spiro-MeO-TPD in a planar cell configuration of ITO/F6-TCNNQ/spiro-MeO-TPD/$CH_3NH_3PbI_{3-x}$-Cl_x/C_{60}/Ag generated J_{sc} = 16 mA cm^{-2}, V_{oc} = 1.03 V, FF = 0.66, and PCE = 10.9%. In another study of fully vacuum-processed planar heterojunction performed by Kim et al.,[73] the employment of HTL (MoO$_3$/NPB) and ETL (C_{60}/BCP) with a double-layer structure was observed to show improved energy level alignments at the interfacial contact resulting in higher V_{oc}. The solar cell with ITO/MoO$_3$/NPB/$CH_3NH_3PbI_3$/C_{60}/BCP/Al planar hetero-junction architecture showed best solar cell parameters of J_{sc} = 18.1 mA cm^{-2}, V_{oc} = 1.12 V, FF = 0.68, and PCE = 13.7%.

3. Hybrid deposition method

Despite the aforementioned advantages of vacuum-based fabrication of perovskite layers and solar cells, difficulties in calibrating the QCM parameters for CH_3NH_3I materials were mentioned in almost all of these studies as a key challenge to achieve reproducible, uniform and stoichiometry controllable perovskite films.[5,37,71,74,75] The evaporation rate of CH_3NH_3I is difficult to calibrate and control because of its relatively high vapor pressure. In addition, CH_3NH_3I is observed to deposit everywhere on the cold surfaces inside the chamber. For instance, the CH_3NH_3I layer was detected (XRD and AFM) on the top surface of a substrate that is facing the opposite direction of the CH_3NH_3I source.[79] In contrast, lead halides were observed to deposit mainly along the line-of-sight direction from the source. The high vapor pressure of CH_3NH_3I also leads to cross-talking to the reading of the QCM that is used to monitor the evaporation rate of lead halides. To solve such a challenge, Qi and co-workers developed a new methodology (the hybrid deposition method) where the perovskite stoichiometry is ensured by controlling the CH_3NH_3I vapor partial pressure inside the vacuum chamber.[78,79] The optimized home-built instrumentation is illustrated in Fig. 7a.[78] A more detailed study on the hybrid deposition method was reported by Wang et al.[79] and is discussed later in this section. The main vacuum chamber (Part #1 in Fig. 7a) is evacuated by using a pumping system consisting of a turbo molecular pump (HiPace 300, Pfeiffer) and a manual gate-valve (10840-CE01, VAT). The substrate holder stage (Part #3) allows stable cooling and heating in the temperature range from −190 °C up to 200 °C and can accommodate a wide range of substrate (Part #4) sizes up to 5 × 5 cm^2. A substrate shutter (Part #5) is mounted just below the substrate. The evaporation rates are monitored by two QCMs (Parts #6 and #7). The first QCM (Part #6) facing downward monitors the PbCl$_2$ evaporation rate while the second QCM (Part #7) facing upward is used to monitor the CH_3NH_3I vapor and avoids the cross-talk from the metal halide source. Two evaporation sources are used for the sublimation of the precursor materials. CH_3NH_3I vapor was produced by a Knudsen cell (Part #8) type source to fill the chamber. It is emphasized that a permanent shutter in front of the Knudsen cell was mounted for avoiding the high flux of CH_3NH_3I reaching directly the substrate, which may cause the non-uniform composition of the film. To achieve a high level of film uniformity in thickness and composition as well as to provide large scale uniform evaporation (5 × 5 cm^2), the PbCl$_2$ is resistively heated from a large dish-shaped crucible (Part #9) with ~3 cm in diameter. The heating element (Part #10) consists of a tungsten wire (ϕ = 0.25 mm) wound into a spiral shape and connected to a power supply through electric feedthroughs (Part #11). The halide shutter (Part #12) allows de-convolution and extrapolation of the lead halide evaporation rate after subtracting the CH_3NH_3I evaporation rate entering in the first QCM (Part #6). The total pressure inside the chamber is monitored by using a full-range (~10^5 to 10^{-7} Pa) pressure gauge (Part #13).

The initial CH_3NH_3I calibration and the determination of the optimized CH_3NH_3I : PbCl$_2$ ratio procedure are similar to the method described by Malinkiewicz et al. (see Section 2).[5,71] However, in the hybrid deposition, because the CH_3NH_3I QCM faces upwards, the QCM parameters are set to values in such a way that the signal-to-noise ratio was reasonable to monitor the CH_3NH_3I during evaporation. The optimized parameters

6700 | J. Mater. Chem. A, 2016, 4, 6693–6713

This journal is © The Royal Society of Chemistry 2016
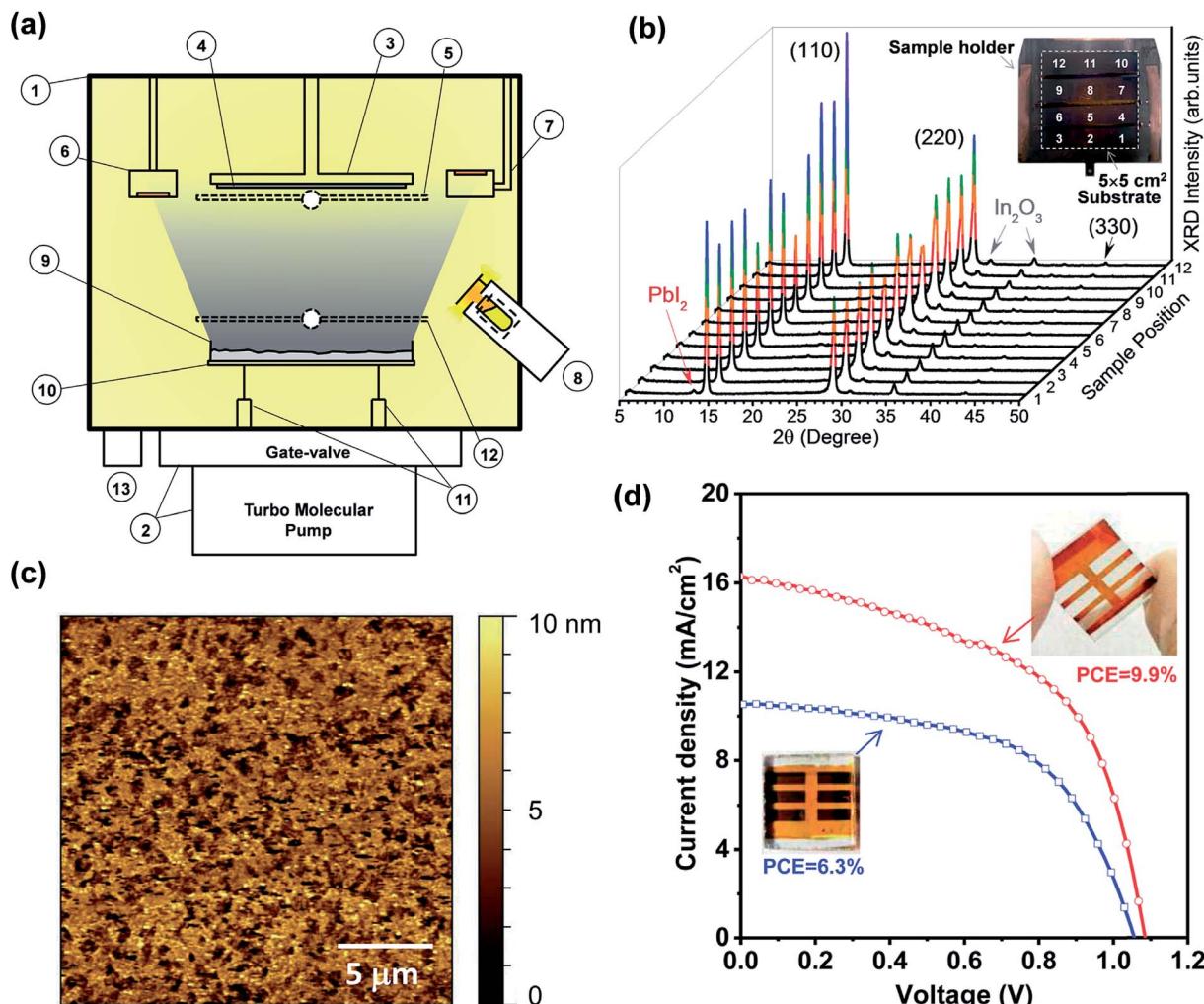
Fig. 7 (a) Side view of the hybrid deposition method system: (1) main vacuum chamber; (2) pumping system comprising a gate-valve and a turbo molecular pump; (3) substrate holder stage which allows cooling and heating from −190 °C to 200 °C; (4) substrate sizes of up to 5 × 5 cm²; (5) substrate shutter; (6) QCM facing downwards; (7) QCM facing upwards; (8) Knudsen cell evaporator for producing MAI vapor partial pressure; (9) widely opened dish-shaped crucible for the evaporation of lead halide compounds; (10) spiral-shaped tungsten wire; (11) electric feedthroughs; (12) lead halide shutter; (13) pressure gauge. (b) XRD and picture of the perovskite film prepared in the hybrid deposition system on a large (5 × 5 cm²) ITO/glass substrate and measured at 12 different points. Note that the as-prepared films show a light orange color. The dark brown color in the picture is from the copper sample holder. (b) XRD and picture of the perovskite film prepared in the hybrid deposition system on a large (5 × 5 cm²) ITO/glass substrate and measured at 12 different points. (c) AFM topography image (scan size: 20 μm × 20 μm) of the perovskite film (∼50 nm) deposited on the ITO substrate from which the surface RMS roughness of ∼4.6 nm was extracted. (d) J–V characteristics of the solar cells based on the perovskite films with two different thicknesses prepared by the hybrid deposition method under AM 1.5G illumination. Solar energy-to-electricity conversions of 6.3% (blue curve) and 9.9% (red curve) were extracted for devices using ∼50 nm and ∼135 nm perovskite films, respectively. Reproduced from ref. 78 with permission of The Royal Society of Chemistry.

were $\rho = 0.2 \text{ g cm}^{-3}$, Z-factor = 0.2, and tooling factor = 100. The absolute amount of CH_3NH_3I inside the chamber cannot be quantified. Therefore, the perovskite deposition conditions ($PbCl_2 : CH_3NH_3I$ ratio) were optimized by depositing several batches of perovskite films with varied CH_3NH_3I nominal rates to identify the evaporation conditions that led to strong XRD peaks measured on perovskite films. In this way, large-area uniformity of the perovskite films (∼135 nm) was demonstrated by measuring XRD patterns at 12 different points on the 5 × 5 cm² deposited film, Fig. 7b. The hybrid-deposited films with ∼50 nm and ∼135 nm perovskite films were observed to show

a uniform semi-transparent light-orange color with a highly reflective (shiny) surface, distinctively different from the black or dark brownish color commonly observed for solution processed samples. Based on AFM measurements the surface roughness values of ∼4.6 nm (Fig. 7c) and ∼9 nm were determined for the ∼50 nm and ∼135 nm perovskite films, respectively.

The centimeter-scale uniform semi-transparent nature of the perovskite films grown by the hybrid deposition method is particularly suitable for large-scale window photovoltaic applications where good transparency and reasonable efficiency are prerequisites.[113,114] The best performing device for the ∼50 nm

perovskite film (Fig. 7d, blue curve) under standard AM1.5G illumination achieved $J_{sc} = 10.5$ mA cm^{-2}, $V_{oc} = 1.06$ V, FF = 0.566, and PCE = 6.3%. On the thicker perovskite film (~135 nm), the measured J–V curve under illumination produced J_{sc}, V_{oc}, FF, and PCE of 17 mA cm^{-2}, 1.09 V, 0.535, and 9.9%, respectively (Fig. 7d, red curve).

Wang et al.[79] performed detailed systematic studies on the perovskite formation using the hybrid deposition method by varying the (i) evaporation source materials (PbCl$_2$: CH$_3$NH$_3$I versus PbI$_2$: CH$_3$NH$_3$I), (ii) substrate temperature, and (iii) post-annealing conditions. The instrumentation was slightly modified to position the CH$_3$NH$_3$I QCM facing downwards and right above the CH$_3$NH$_3$I evaporation source to enhance the evaporation rate detection for CH$_3$NH$_3$I. A shutter was placed between the CH$_3$NH$_3$I QCM and evaporation source. With this new geometry, the authors were able to better control the CH$_3$NH$_3$I rate by the QCM over a long deposition period (~1 h). This shows that the evaporation of CH$_3$NH$_3$I cannot be treated as standard line-of-sight evaporation (e.g., PbI$_2$ or PbCl$_2$) and significant optimization in the system is needed for the better control of the CH$_3$NH$_3$I vapor inside the chamber during perovskite formation. Based on the PbCl$_2$: CH$_3$NH$_3$I versus PbI$_2$: CH$_3$NH$_3$I studies, the following reaction steps are proposed to take place for the perovskite film formation under the vacuum conditions.

$$PbCl_2 + 2CH_3NH_3I \rightarrow 2CH_3NH_3Cl + PbI_2 \quad (R1)$$

$$PbCl_2 + CH_3NH_3Cl \rightarrow CH_3NH_3PbCl_3 \quad (R2)$$

$$PbI_2 + CH_3NH_3I \rightarrow CH_3NH_3PbI_3 \quad (R3)$$

In the PbCl$_2$: CH$_3$NH$_3$I deposition case when excessive PbCl$_2$ is present, reactions (R1) and (R2) occur, forming a pure CH$_3$NH$_3$PbCl$_3$ phase. As the ratio of PbCl$_2$: CH$_3$NH$_3$I reduces, the films are composed of phase segregated CH$_3$NH$_3$PbCl$_3$ and CH$_3$NH$_3$PbI$_3$ perovskites via reactions (R1), (R2), and (R3). When the PbCl$_2$: CH$_3$NH$_3$I ratio was further decreased matching stoichiometry, only the pure CH$_3$NH$_3$PbI$_3$ perovskite phase was observed to form and corroborated by XRD and X-ray photoelectron spectroscopy (XPS). This is also consistent with the solution-processed perovskite films where no XPS Cl 2p signal was found in the bulk perovskite film and only 1% Cl could be detected at the bottom 20 nm of the film.[26] Therefore, the chemical formula of "CH$_3$NH$_3$PbI$_3$" was more precise to be represented than "CH$_3$NH$_3$PbI$_{3-x}$Cl$_x$" in the perovskite films formed from PbCl$_2$ + CH$_3$NH$_3$I precursors. In the PbI$_2$: CH$_3$NH$_3$I deposition case, only reaction (R3) takes place. The excess of PbI$_2$ is readily detected in XRD with a characteristic 12.6° peak, which corresponds to the PbI$_2$. On the other hand, excess of CH$_3$NH$_3$I was observed to generate the characteristic peaks at 9.7°, 19.6°, and 29.6°. An additional peak at 11.4° was observed to evolve as a function of air exposure time and associated with the H$_2$O-incorporated perovskite (complex formation). No significant morphology differences were observed in the optimized perovskite films deposited from PbCl$_2$: CH$_3$NH$_3$I and PbI$_2$: CH$_3$NH$_3$I cases showing surface roughnesses of 24.5 nm

and 26.5 nm, respectively, measured by AFM. It is interesting to note that in the PbCl$_2$: CH$_3$NH$_3$I case, stronger preferred orientation along the (110) plane of CH$_3$NH$_3$PbI$_3$ was observed to form compared to that of the PbI$_2$: CH$_3$NH$_3$I case. It has been proposed that the additional intermediate CH$_3$NH$_3$Cl species formed (R1) from the PbCl$_2$: CH$_3$NH$_3$I evaporation help slow down the reaction kinetics for the final CH$_3$NH$_3$PbI$_3$ formation.[26,115] In the recent work by Teuscher et al.,[80] a proportional-integral-derivative (PID) driven thermal evaporator was developed in their vacuum chamber allowing a more precise control of the PbI$_2$: CH$_3$NH$_3$I stoichiometric ratio as well as improving reproducibility. The composition of the deposited materials was quantitatively analyzed using inductively coupled plasma mass spectrometry (ICP-MS) and the PbI$_2$: CH$_3$NH$_3$I ratio of 1 : 0.96 resulted in the best performing solar cell devices (device structure: FTO/TiO$_2$ compact layer/perovskite/spiro-MeOTAD/Au): $J_{sc} = $ ~18 mA cm^{-2}, $V_{oc} > 1.1$ V, FF > 0.7, and PCE > 12%.

The growth of the perovskite film was highly dependent on the substrate temperature during deposition, mainly influenced by the sticking coefficient of CH$_3$NH$_3$I vapor. The low substrate temperature (−50 °C) led to a high sticking coefficient, but a poor quality perovskite film with partial coverage. At higher temperatures (>80 °C), films with excess PbI$_2$ and intermediate phases were observed and associated with the lower sticking coefficient of CH$_3$NH$_3$I vapor. The optimum substrate temperature was 20 °C, which generated growth of perovskite films with high crystallinity and full coverage.

Solution-processed perovskite films generally require the post-annealing treatment (80–120 °C) for efficient conversion from the precursors to perovskite and to ensure vaporization of the solvent and subsequent crystallization.[94,95] On the other hand, Malinkiewicz et al.[5,71] have shown that post-annealing is not required in vacuum-processed perovskite films, yet attain high solar cell efficiencies. Wang et al.[79] performed detailed post-annealing studies on non-stoichiometric and stoichiometric perovskite films formed by the hybrid-deposition method. It is shown that post-annealing is beneficial for the perovskite films with excessive CH$_3$NH$_3$I. Gentle annealing in an N$_2$ environment at 110–120 °C helps desorb the undesirable H$_2$O-incorporated complex. High temperatures (>130 °C) decompose the CH$_3$NH$_3$PbI$_3$ to PbI$_2$. The post-annealing at 120 °C for 1 h in an N$_2$ environment on a perovskite film with stoichiometric composition was observed to have a negligible effect on the crystallinity and morphology of the film probed by XRD and AFM. This is in good agreement with the device performance that shows nearly the same PCE compared to that of the identically prepared cells (same deposition batch), but one with and the other without the post-annealing treatment. In this work, the solar cells based on optimized perovskite films as thin as ~170 nm generated J_{sc}, V_{oc}, FF, and PCE of 19.92 mA cm^{-2}, 1.098 V, 0.524, and 11.48%.[79] The high V_{oc} (over 1 V) typically achieved by the hybrid deposition[78,79] is well aligned with the reported values using vacuum-deposition methods: 1.07 V in the work of Liu et al.[4] and 1.05 V in the work of Malinkiewicz et al.[5] On the other hand, solution processed ones have generally substantially lower V_{oc} possibly due to the large

variations of the film morphology.[4] The pin-hole free uniform perovskite layer prevents shunting pathways effectively, leading to a lower recombination rate.[52,116,117] In a recent work by Zhao et al.,[81] vacuum-processed perovskite solar cells with an ultra-thin metal-oxide free and annealing-free C_{60} or C_{70} as the ETL was demonstrated to generate high PCEs (Table 1).

4. Hybrid chemical vapor deposition

Chemical Vapor Deposition (CVD) is a scalable technology that uses batch processing to generate throughput sufficient for industrial applications, and is used for a wide variety of material deposition. CVD is often performed with a tube furnace, where the temperature, gas environment, and flow rate can be well controlled. Perovskite film growth by a CVD process was first demonstrated in 2014,[82] and can be differentiated from other vapor deposition processes that are more direction dependent and require higher vacuum conditions. CVD relies more on thermally driven diffusion, which can transport material to substrates regardless of substrate orientation. Typically perovskite growth by CVD uses an inert carrier gas such as nitrogen or argon to provide an oxygen and water free environment, but has been demonstrated using air as well.

Ambient pressure thermal diffusion driven perovskite film growth was first demonstrated using VASP with the PCE up to 12.1%.[62] In this system lead iodide was first deposited onto substrates, which were then loaded into a heated (150 °C), closed container with CH_3NH_3I. The time required for complete conversion was approximately 2 h. This is essentially a 2-step CVD process with nitrogen gas at atmospheric pressure. A similar ambient pressure perovskite growth was reported, but used a CVD tube furnace (145 °C) and ambient air, which demonstrated maximum PCE of 12.2%.[84] This process also required 2 h for complete conversion.

Lower pressures increase the rate of diffusion and the rate of sublimation of organic halide, therefore low pressures allow for greater uniformity, faster deposition rates or the use of lower temperatures. Low pressure CVD growth was first demonstrated using a 2-step process using $PbCl_2$, and a two zone furnace, which demonstrated up to 11.8% PCE.[82] One zone was dedicated to CH_3NH_3I (185 °C) and the other to substrates (145–170 °C), with pressures of 100 Pa using nitrogen carrier gas. Note that perovskite film properties strongly depend on the process temperature, and therefore precise temperature measurements close to the source or substrates inside the tube furnace can provide valuable insight for process optimization. Two zone deposition allows for faster deposition because the vapor pressure of the organic halide can be controlled independent of the substrate. The nominal reaction time reported was 1 h. A later paper by the same group using formamidinium iodide show perovskite conversion with less than 30 min of heating the organic component and an efficiency of 14.2%.[83] This suggests that the deposition times can be shortened, which is desirable for industrial processes. The typical film roughness of perovskite samples is 20–40 nm, and the films are semitransparent. Similar work using a low pressure 2-zone furnace was performed by different authors, but without the use of nitrogen carrier gas and

at a slightly lower substrate temperature (140 °C) to achieve a PCE of 12.7%.[85] However, the pressure was not specified. The highest performing reported solar cell fabricated by CVD (15.1%) used a low vacuum (100 Pa) and single zone furnace (140 °C) with 2–3 h deposition time.[118] Low pressures can be used to reduce the required reaction temperature, because the sublimation temperature of organic halide is reduced at lower pressures. High performing cells were fabricated at ~0.3 Pa and 82 °C reaching a PCE of 14.7%.[119] However, a long reaction time of 3 h was required for complete conversion at low temperatures.

It was consistently observed that longer deposition times could be detrimental to solar cell performance, even in cases when XRD crystallinity was enhanced.[83,118] There are several possible reasons for the decrease in performance. It is possible that longer deposition times produce an excess of organic halide, which then can act as insulating contaminant in the solar cell, or can lead to more hygroscopic surfaces causing rapid decay of the cell from water absorption. In the case of chlorine-containing perovskite, longer deposition times can cause depletion of chlorine, which is believed to cause shorter carrier lifetimes and lower PCE.[83] In the case of formamidinium perovskite, the excess organic component is easily absorbed in the perovskite thin film, creating a different crystal structure. The excess can be desorbed by annealing, but the modification of the crystal structure was observed to negatively impact the grain size and reduce performance.[83]

Most processes for perovskite solar cell fabrication used a 2 step process for perovskite growth. There is a significant difference in temperature between the evaporation temperature of metal halide and organic halide, and therefore it is difficult to uniformly deposit both layers at the same step. Most reports that deposited both layers by CVD formed discontinuous films. This is not ideal for solar cells, but can be useful for optoelectronics devices. For instance, perovskite nano-platelets,[120,121] and nano-wires[122] can be used for laser applications. Another type of single step CVD process used aerosol-assisted chemical vapor deposition for the formation of discontinuous perovskite thin films.[123,124] One work fabricated solar cells by single step CVD and produced efficiencies up to 11.1%.[125] The advantage of using a single step approach is clear as long as uniformity is sufficient across a batch.

Solar cells prepared by a CVD process typically had reasonably high stability compared to some solution processed methods.[82,83,118,119] Solution processed samples can decay even in an inert, dark environment,[50] but CVD cells kept under similar conditions were reported to be stable and even improved in efficiency over time. As the solar cell aged the V_{oc} increased, while the J_{sc} decreased resulting in a small net gain for the PCE.[82,83,118,119] However, it is possible that this behavior is specific to cells using spiro-MeOTAD as the hole transport medium. When kept in air, CVD solar cells were reported to decay from 14.7% to 12.1% over the course of 30 days.[119] This prolonged stability is possibly due to high temperatures during perovskite formation (less chemical and/or phase impurities) or the absence of solvent usage (e.g. DMF, DMSO) that can get incorporated into solution processed perovskite films. However, few papers directly addressed stability under operational conditions, but it is mentioned that solar cells under continuous irradiation decay faster than cell with periodic measurements.[118]

This journal is © The Royal Society of Chemistry 2016

J. Mater. Chem. A, 2016, 4, 6693–6713 | 6703
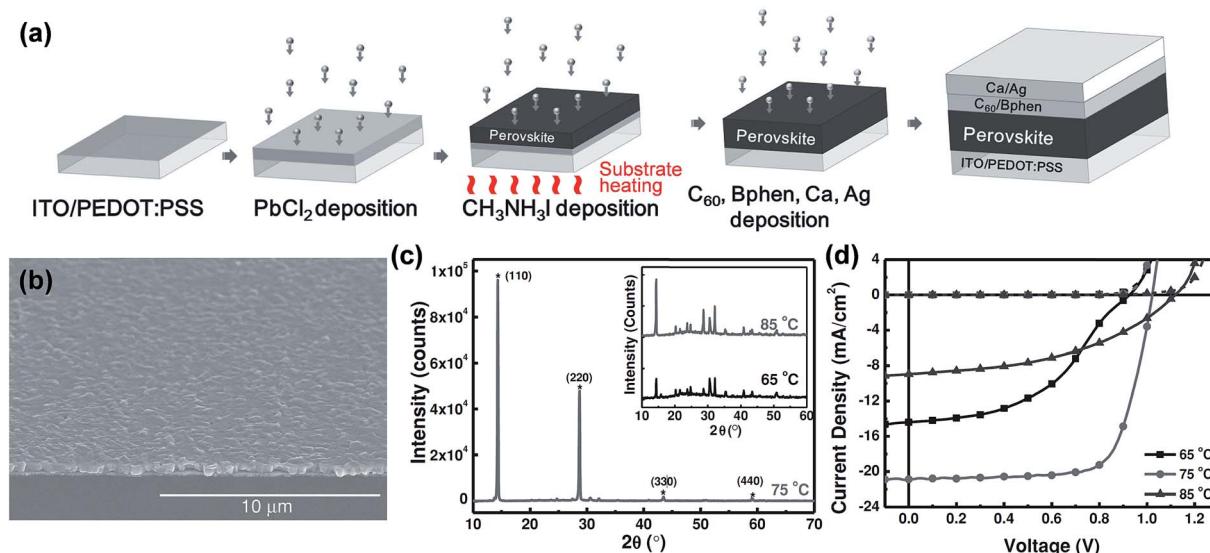
Fig. 8 (a) Schematic illustration for the fabrication of perovskite solar cell employing sequential layer–by–layer vacuum deposition. (b) Large area SEM image of the $CH_3NH_3PbI_{3-x}Cl_x$ thin film fabricated with the substrate temperature held at 75 °C during CH_3NH_3 sublimation. (c and d) XRD and $J-V$ characteristics of perovskite layers and solar cells with varying substrate temperatures (65 °C, 75 °C, 85 °C) during CH_3NH_3 sublimation. Reproduced with permission from ref. 88.

5.   Vacuum sequential deposition

General difficulties in co-evaporation methods are often associated with the need for careful and simultaneous control of evaporation rates of both precursors (lead halides and methylammonium halides) to achieve uniform stoichiometry in the deposited films. In this sense, the one-material-at-a-time deposition method has a big advantage for easy control of the evaporation rates of the individual sources.[126] Chen *et al.*[88] reported planar structured perovskite solar cells by the sequential layer-by-layer vacuum deposition method attaining a PCE as high as 15.4%, Table 1. Their devices were prepared using indium-doped tin oxide (ITO) spin-coated coated with PEDOT:PSS. Subsequently, the substrates were loaded into a high vacuum chamber (base pressure $< 1 \times 10^{-6}$ Torr) to evaporate $PbCl_2$, CH_3NH_3I, C_{60}, bathophenanthroline (Bphen), Ca, and Ag. Except for the CH_3NH_3I deposition, the substrate temperature was maintained at room temperature during deposition of all other layers ($PbCl_2$, C_{60}, Bphen, Ca, Ag), Fig. 8a. The substrate temperature while sublimating CH_3NH_3I was found to be critical for the photovoltaic performance, Fig. 8b and c. Photovoltaic performance was the highest when the substrate was heated to 75 °C and compared to those where the substrate temperature was maintained at 65 °C and 85 °C during CH_3NH_3I deposition, Fig. 8d. The thickness of the perovskite film was determined to be proportional to the initial thickness of the $PbCl_2$ layer. The film thickness expansion ratio of ∼1 : 2.9 was reported when $PbCl_2$ is converted to $CH_3NH_3PbI_{3-x}Cl_x$. All the optimized films (thickness ∼ 430 nm) were reported to have smooth surfaces with surface RMS roughnesses of 24.1 nm, 22.7 nm, and 23.3 nm for substrate temperatures of 65 °C, 75 °C, and 85 °C, respectively. The smoothness of the perovskite films for all temperatures was attributed to the typical ultra-smooth nature of the starting $PbCl_2$

film (RMS roughness ∼7.8 nm). When CH_3NH_3I was deposited on the $PbCl_2$ coated substrate kept at room temperature, the CH_3NH_3I diffusion depth was limited to less than 25 nm leaving the bottom $PbCl_2$ layer unreacted leading to decreased PCEs.[88]

Ng *et al.*[90] have employed the deposition of both PbI_2 and CH_3NH_3I at room temperature by decreasing the thickness of both precursor layers. However, an additional subsequent thermal annealing step was necessary for the full conversion to $CH_3NH_3PbI_3$ perovskite. A multilayered structure consisting of seven alternating depositions of PbI_2 (50 nm)/CH_3NH_3I (50 nm) pairs with subsequent annealing in N_2 gas (90 °C, 1 h) generating a $CH_3NH_3PbI_3$ perovskite film with ∼473 nm thickness and surface roughness of ∼20 nm exhibited the highest average solar cell parameters: $J_{sc} = 20.0 \pm 0.8$ mA cm^{-2}, $V_{oc} = 1.00 \pm 0.03$ V, FF = 0.57 ± 0.02, and PCE = 11.4 ± 0.5%. Planar structured perovskite solar cells were composed of glass/FTO/c.l.-TiO$_2$/$CH_3NH_3PbI_3$/spiro-MeOTAD/MoO$_3$/Al layers. The same group of authors investigated the impact of dry-O_2 annealing[127] of the thermally evaporated $CH_3NH_3PbI_3$-based solar cells. The results suggested that O_2-treatment helped enhance the solar cell performance. Under the optimized conditions, the champion device exhibited: $J_{sc} = 21.8$ mA cm^{-2}, $V_{oc} = 0.96$ V, FF = 0.60, and PCE = 12.5%.[90] Low-temperature (max. of 100 °C) fabrication of hole-conductor-free planar perovskite solar cells consisting of only a $CH_3NH_3PbI_3$/C_{60} bilayer structure was reported by Hu *et al.*[89] to generate a PCE of 5.4%. Abbas *et al.*[91] have fabricated $CH_3NH_3PbI_3$ perovskites through sequential deposition of PbI_2 in vacuum and subsequently to CH_3NH_3I after transferring the samples to a graphite vessel. The solar cell devices with FTO/c.l.-TiO$_2$/$CH_3NH_3PbI_3$/P3HT/Au structure and after optimization of the P3HT layer (thickness ∼ 30 nm and polymer concentration ∼ 12 mg ml^{-1}) have generated high solar cell parameters: $J_{sc} = 21.76$ mA cm^{-2}, $V_{oc} = 0.96$ V, FF = 0.653,
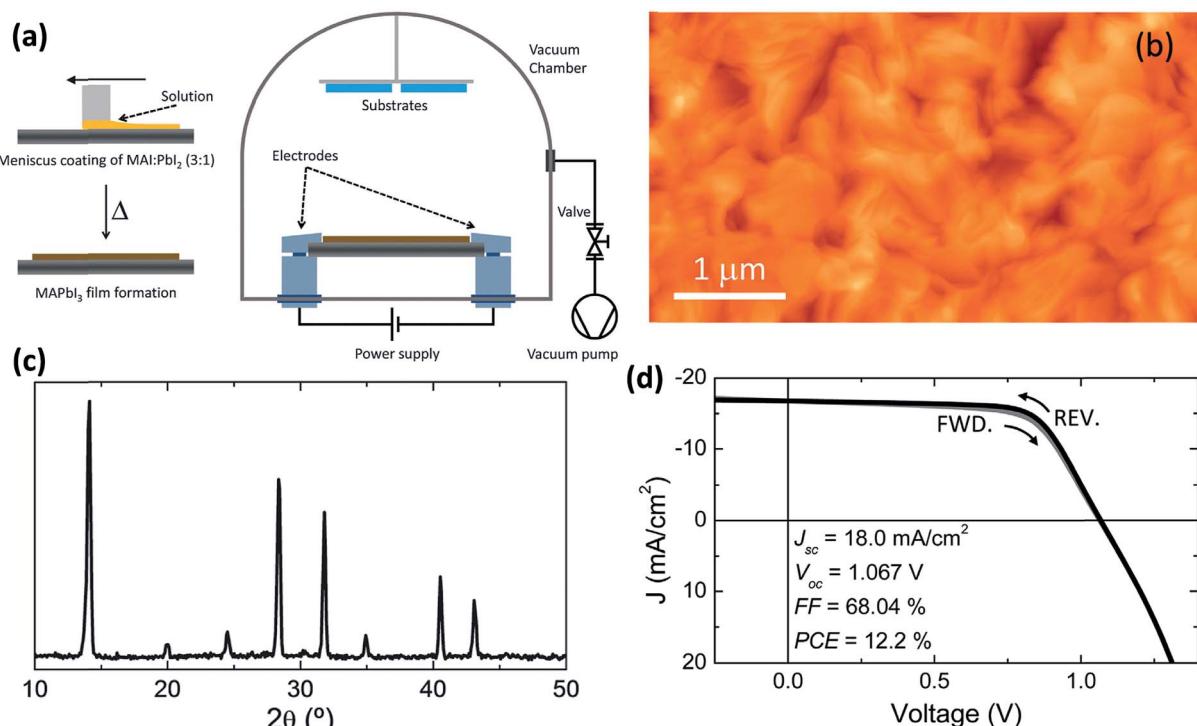
Fig. 9 (a) Schematic illustration of the fabrication of perovskite films employing flash evaporation. The precursor solution is spread onto a tantalum foil and mildly annealed obtaining a polycrystalline $CH_3NH_3PbI_3$ film. The coated tantalum heater is transferred to a vacuum chamber ($\sim$0.1 mbar) where the perovskite is evaporated onto the desired substrate by passing a high current ($\sim$30 A). (b and c) AFM topography and GIXRD pattern of the flash evaporated $CH_3NH_3PbI_3$ film. (d) $J-V$ characteristics in forward (FWD) and reverse (REV) bias scans for a device with the ITO/PEDOT:PSS/$CH_3NH_3PbI_3$/polyTPD/PCBM/Ba/Ag structure and under illumination. Reproduced from ref. 93 with permission of The Royal Society of Chemistry.

and PCE = 13.7%.[91] More recently, Yang et al.[92] have demonstrated solar cell devices with large active areas of 1 cm^2 that exhibit a high PCE of 13.84%, by the alternating layer-by-layer ($PbCl_2$/CH_3NH_3I) vacuum deposition technique.

Atomic layer deposition (ALD) can be another suitable technique for automatizing the sequential deposition of alternating layers of precursors. ALD is a low-vacuum and low-temperature deposition technique capable of uniform, conformal growth of films over large area with atomic thickness precision. Although, at present, there are no direct processes for the growth of OHPs fully by ALD, alternative protocols have been proposed by Sutherland et al., who showed enhanced optoelectronic properties of ALD processed OHP layers.[128,129]

6. Flash evaporation or single-source thermal ablation technique

The concept of flash evaporation was first described by Harris and Siegel in 1948 demonstrating the evaporation of metal alloys with controlled stoichiometry.[130] Later on, the method was applied for the evaporation of inorganic semiconductor alloys[131] as well as oxide-based perovskite materials.[132] In 1999, Mitzi et al.[97,133] demonstrated that the same technique could be applied for the fabrication of OHP films (named as single source thermal ablation technique). Briefly, the OHP material is initially synthesized by solution processing and spread on

a metal heater (e.g. tantalum or molybdenum), Fig. 9a. The dried OHP and heater are loaded into a vacuum chamber. After the system is pumped to vacuum, a large current is passed through the heater causing the OHP material to rapidly evaporate and condense onto a substrate. The desired OHP films are formed when the material is heated rapidly and at high enough temperatures, causing sublimation of the entire compound without thermal decomposition of the organic constituents, Fig. 9a.[93,97,133–136] Longo et al.[93] have synthesized $CH_3NH_3PbI_3$ perovskite films by using the flash evaporation technique and showed that smooth surface morphology was obtained with a surface RMS roughness of $\sim$17.6 nm, Fig. 9b. GIXRD measurements confirmed the formation of stoichiometric $CH_3NH_3PbI_3$ and revealed high degree of crystallinity, Fig. 9c. Solar cell devices with ITO/PEDOT:PSS/$CH_3NH_3PbI_3$/polyTPD/ PCBM/Ba/Ag layers in a planar heterojunction structure showed respectful solar cell parameters of J_{sc} = 18 mA cm^{-2}, V_{oc} = 1.067 V, FF = 0.68, and PCE = 12.2%.[93]

7. Fundamental understanding of OHP films prepared by vacuum processing

In parallel to several studies focusing on improving the device performance, equal effort has also been made to address the fundamental aspects of the device physics and chemistry. This

This journal is © The Royal Society of Chemistry 2016

J. Mater. Chem. A, 2016, 4, 6693–6713 | 6705

Journal of Materials Chemistry A

View Article Online

Review

Open Access Article. Published on 01 December 2015. Downloaded on 2/15/2026 6:51:35 AM. This article is licensed under a Creative Commons Attribution 3.0 Unported Licence.
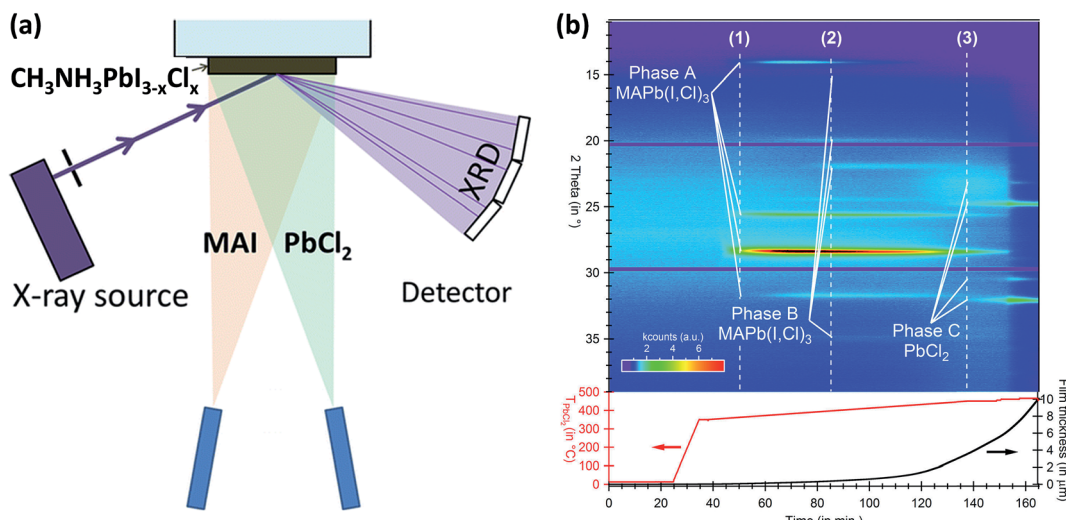
Fig. 10 (a) Schematic illustration of the design of a vacuum chamber for perovskite thin film deposition by the multisource evaporation and *in situ* XRD setup for the real-time monitoring of crystalline phase formation. (b) Time evolution representation of the X-ray diffracted intensity measured during $CH_3NH_3PbI_{3-x}Cl_x$ formation. The CH_3NH_3I (MAI) source was operated at a constant temperature of 110 °C. The temperature ramp of the $PbCl_2$ source (T_{PbCl_2}) and the film thickness are indicated. Three different crystalline phases named A, B, and C are detected according to the $PbCl_2$: MAI flux ratio and marked with dotted lines (1), (2), and (3), respectively. Reprinted with permission from ref. 151. Copyright (2014) American Chemical Society.

section is intended to summarize the fundamental understanding earned from the vapor-processed OHPs and solar cells and describe the remaining open questions in this field.

The majority of the fundamental aspects of perovskites come from reports on solution-processed perovskites.[26,54,112,137–150] Vapor-based systems used for the OHP film synthesis offer unique advantages, *i.e.*, they are compatible with surface science analytical tools and *in situ* studies. *In situ* monitoring allows the investigation of events taking place in the OHP films, *e.g.* during formation or degradation, without altering its pristine conditions that can be influenced by the environmental conditions (*e.g.* H_2O, O_2, temperature, light, *etc.*). In addition, it allows systematic investigation of the influences of controlled environmental conditions (*e.g.* humidity, O_2, temperature, light, *etc.*) on the material system under study. Pistor *et al.*[151,152] have used a dedicated vacuum chamber system where perovskite film crystalline phase formation from the co-evaporation of $PbCl_2$ and CH_3NH_3I sources could be monitored *in situ* and real-time by a built-in XRD setup, Fig. 10a. The $PbCl_2$: CH_3NH_3I flux ratio was observed as a key parameter for the formation of perovskite films with distinct crystalline phases, Fig. 10b. The CH_3NH_3I (MAI) source was heated at a constant temperature of 110 °C. The temperature ramp of the $PbCl_2$ source (T_{PbCl_2}) was increased steadily from 350 °C to 465 °C. Under low $PbCl_2$ flux conditions, marked with a dotted line (1) in Fig. 10b, the formation of a dark gray/brown $CH_3NH_3PbI_{3(1-y)}Cl_{3y}$ film with diffraction peaks at 14.046°, 28.332°, and 31.69°, phase (A), was characteristic. Additional energy dispersive X-ray spectroscopy (EDX) and optical transmission/reflection measurements revealed films with low chlorine content ($y = \sim0.02$–0.05) and a bandgap of ~1.6 eV. At higher $PbCl_2$ flux, dotted line (2) in Fig. 10b, XRD revealed formation of a second crystalline phase (B) with peaks at 15.40°, 19.71°, 21.89°, and

35.05°. A chloride-rich phase was identified ($y \sim 1$) by EDX with films appearing greenish and transparent. A further increase in temperature of the $PbCl_2$ crucible generates films with pure $PbCl_2$ composition, dotted line (3) in Fig. 10b. In contrast to the Br–I mixed perovskites ($CH_3NH_3PbI_{3(1-z)}Br_z$) where the formation of solid solution over the whole range ($0 < z < 1$) was reported,[153] the authors of this study concluded that mixed $CH_3NH_3PbI_{3(1-y)}Cl_y$ perovskites are not stable for all mixtures between $CH_3NH_3PbI_3$ and $CH_3NH_3PbCl_3$. The authors estimated this miscibility gap to be in the range of $0.02 < y < 0.5$ and explained it by the increasing difference in the I^-–Br^-–Cl^- ionic radii and was demonstrated by Mosconi *et al.*[154] using first-principle calculations. Ng *et al.*[76] have also studied the formation chemistry of mixed $CH_3NH_3PbI_{3-x}Cl_x$ perovskites by *in situ* XPS. $PbCl_2$ was evaporated layer by layer with an increasing total thickness on top of a CH_3NH_3I film (15 nm) pre-deposited on ITO and XPS Pb 4f, Cl 2p, C 1s, and N 1s core levels were monitored as a function of the $PbCl_2$ thickness. During the initial deposition (0.2 nm to 0.5 nm) the Pb signal was detected, but no Cl signal was observed taking into account the detection limit of the XPS measurement ($\sim\pm0.1$ atm%). The Cl signal is only observed for a $PbCl_2$ film thickness above 1 nm indicating that $PbCl_2$ can be included when away from the $CH_3NH_3I/PbCl_2$ interface. The absence of Cl at the $CH_3NH_3I/PbCl_2$ interface ($PbCl_2$ thickness below 0.5 nm) was attributed as a result of the interaction between $PbCl_2$ and CH_3NH_3I where Cl^- is energetically unfavorable because of the abrupt difference in the ionic radii of Cl^- and I^- ions.[154] These results are also consistent with the low content of chloride identified in solution processed $CH_3NH_3PbI_{3-x}Cl_x$ perovskite films.[26,155,156]

The formation mechanism of pure $CH_3NH_3PbI_3$ perovskite was studied by Liu *et al.*[157] using *in situ* XPS on successive depositions of thermally evaporated CH_3NH_3I on a pre-formed

6706 | *J. Mater. Chem. A*, 2016, **4**, 6693–6713

This journal is © The Royal Society of Chemistry 2016
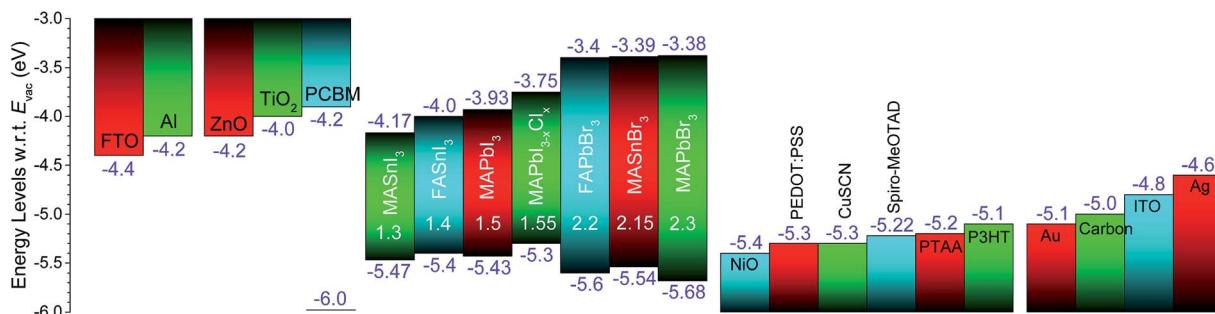
Fig. 11 Summary of literature values for the energy levels with respect to (w.r.t.) the vacuum level (E_{vac}) for the different materials acting as anode and cathode electrodes, electron transport layer, OHP, and hole transport layer. The optical bandgaps are indicated below each type of OHPs. Variations in HOMO, LUMO, and band edge positions are observed in the literature. It is emphasized that the flat band assumption does not hold true when two layers are brought in contact. Reproduced from ref. 18 with permission of The Royal Society of Chemistry.

PbI_2 film with focus on the double C 1s feature observed, while only one N 1s species was present. The peaks observed at 286.6 eV and 402.7 eV in the BE scale were assigned to the photo-electrons originated from C and N elements in $CH_3NH_3PbI_3$ perovskite. The low-BE feature at 285.3 eV in C 1s was assigned to CH_3I from the dissociation of CH_3NH_3I to CH_3I and NH_3. In fact, the assignment of the low-BE feature is still under debate. Ng et al.[158] and Li et al.[159,160] have also identified more than one peak in the C 1s region and assigned the low BE feature to amorphous carbon (C–C).

Li et al.[160] performed in situ XPS and investigated the degradation of co-evaporated $CH_3NH_3PbI_3$ perovskite films under a controlled environment of dry-O_2, and H_2O exposures conducted in the vacuum chamber by the aid of high-precision leak-valves. $CH_3NH_3PbI_3$ was reported to be not sensitive to O_2 even at higher exposures of 10^{13} Langmuir (L, $1\,L = 10^{-6}$ Torr s). However, a reaction threshold of $\sim 2 \times 10^{10}$ L was found for H_2O exposure proposing decomposition of $CH_3NH_3PbI_3$ to NH_3, HI, and PbI_2 in agreement with previous reports.[161,162]

One important requirement for attaining high-efficiency OHP solar cells is to match the electronic energy levels of OHP absorber and the adjacent selective contacts (ETL and HTL) for minimal energy loss and reduced charge recombination.[112,142,146] A large collection of energy levels with respect to (w.r.t.) vacuum for the different materials commonly employed in OHP-based solar cells is shown in Fig. 11.[17,18,163] The indicated bandgap values for OHPs in Fig. 11 correspond to optical bandgaps (that differs from the transport gap) and all of studies were reported on solution-processed OHPs.[164] Few studies exist on the determination of energy levels on vacuum-processed perovskites measured by UPS.[157,159,160] The flat band assumption widely considered can still provide a rational judgement when choosing functional layers to be coupled with the OHP layer. However, careful determination of band bending, interfacial states, and interfacial dipoles is important when considering the band alignments of OHP layers with adjacent functional layers.[112,142,146,147] In this sense, film deposition by vacuum-methods is suitable for studying the energy alignments because step-wise deposition with controlled incremental amounts of film thickness can be conducted as well as it is directly compatible with UPS and IPES systems. Energy level diagrams

at interfaces were determined for the following material systems: CH_3NH_3PbX/spiro-MeOTAD (X = I_3, $I_{3-x}Cl_x$, Br_3),[112] $CH_3NH_3PbI_3$/C_{60},[139] $CH_3NH_3PbI_3$/Au,[139,145] $CH_3NH_3PbI_3$/MoO_x,[142,144] $CH_3NH_3PbI_3$/copper phthalocyanine (CuPc),[147] $CH_3NH_3PbIBr_2$/spiro-MeOTAD,[142] $CH_3NH_3PbIBr_2$/N,N'-di(naph-thalene-1-yl)-N,N'-diphenylbenzidine (NPB),[142] $CH_3NH_3PbIBr_2$/copper-hexadecafluorophtalocyanine ($F_{16}CuPc$),[142] and $CH_3NH_3PbIBr_2$/1,4,5,6,8,11-hexaazatriphenylene hexacarbonitrile (HAT-CN).[142]

Hysteresis appears as a manifestation in the J–V curves, where its shape is strongly influenced by the scan direction (forward versus reverse), scan rate, scan history, pre-illumina-tion, and pre-biasing conditions.[165–170] It is pointed out that hysteresis in OHP-based solar cells will lead to inaccurate reporting of PCEs, leading to inaccuracies when comparing the different reported PCEs among different laboratories. Stabilized power output under working conditions has been suggested as a useful parameter.[165] Efforts have been made on determining the origins of the hysteresis phenomena. Recently, several studies have enforced to ion migration as the main phenomena in determining charge transport in OHP materials.[8,170–176] Few studies reported on the hysteresis-free J–V characteristics in vapor-processed OHP solar cells.[71,85,88,91,93,177] However, its origin is difficult to be understood from the reported studies as systematic studies are lacking.

8. Conclusions and outlook

The identification of new properties in novel materials is key for generating new technologies. The introduction of well-estab-lished inorganic or organic materials led to dramatic improve-ments in the history of technology. Inorganic silicon-based technology enabled unprecedented development of advanced electronic devices (e.g. laptops, smart phones, digital cameras, Si solar cells, etc.). Organic semiconductors on the other hand have received attention in light-weight, flexible, flat-panel-display and organic light emitting diode applications. The past few years have witnessed a rapid evolution of hybrid organic–inorganic OHP-based solar cells. OHP materials effectively combine the properties of the inorganic framework and the intercalated organic species. As has been reviewed previously,

OHP materials show several desirable properties for photovoltaic[178–180] and other optoelectronic technologies:[181–183] high absorption coefficients, long carrier diffusion lengths, ambipolar carrier transport, shallow defect levels, emission efficiency, and low concentration of defects. Although the operation of vapor based methods often require a certain level of vacuum that is generally perceived as high cost processing, they have been widely employed in the semiconductor industry demonstrating high throughput and reliability. Therefore, a detailed factual cost analysis would be required for evaluating various fabrication methods taking into account the cost-effectiveness in a mass production scenario.[184–186]

When transferring solar cell technology from laboratory scale fabrication know-how to industry-scale production, fabrication cost, efficiency, and lifetime are the three major factors, which are associated together with functionality (e.g. transparency, flexibility, easy integration in tandem cells, etc.).[185,187,188] At this stage, despite the superior quality of films prepared by the vapor-deposition method (e.g. uniform and full coverage),[4] best efficiencies achieved for OHP solar cells based on vapor-based methods (a PCE of 16.5% with an active area of 0.2 cm^2),[37] (Table 1) are still somewhat lower than that of the solution-processed cells (a certified PCE of 20.1%). The efficiencies of vapor deposition based perovskite solar cells are still lagging behind their counterpart prepared by solution based methods. On the other hand, we regard this more as a strong motivation to invite more research effort on vapor based methods, rather than an intrinsic disadvantage associated with vapor based methods. Since the ground-breaking work by the groups of Prof. Snaith and Prof. Bolink in 2013 on vapor deposition prepared perovskite solar cells, more and more research groups became interested and have been making contributions to this topic. For example, at this stage it has been demonstrated by a number of groups that vapor based methods provide another viable route to fabricate perovskite solar cells

leading to promising efficiencies using both regular and inverted structures (see Table 1 and Fig. 12). Efficiencies as high as 16.5% have been reported so far and the trend of efficiency increase is very clear as shown in Fig. 12. Further improvements on the performance of vapor deposition based perovskite solar cells may come from the following strategies. First of all, multiple reports have indicated that the properties of vapor deposition based perovskite are distinctively different from those prepared by solution processing. Therefore, it is necessary to carry out more in-depth investigations on vapor deposition based perovskite films. Secondly, due to the property difference, the optimal fabrication conditions for vapor deposition based perovskite solar cells are most likely not the same as those for solution prepared ones. A complete set of optimization processes hopefully will provide further efficiency growth of vapor deposition based perovskite solar cells. Thirdly, vapor deposition based perovskite films have some specific advantages, e.g. high degree of uniformity (even at relatively thin film thicknesses) and semitransparency, which may provide the vapor based methods with unique features beyond the pure efficiency considerations. Note that none of the PCE values reported in Table 1 has been certified, which to some degree also underscores the need to further explore these vapor-based methods. In general, caution should be practiced when comparing the cell performance reported by different laboratories as PCE values in OHP solar cells are shown to strongly depend on measurement conditions, such as the voltage-scan polarity (forward versus reverse) and rate, light-soaking, pre-biasing, and cell temperature.[168,189] OHP films deposited by vapor-based methods generally show low XRD intensity, but the corresponding solar cells still show relatively high efficiencies. No direct correlation has been reported between XRD peak intensity (generally considered as a measure of crystallinity) and the corresponding solar cell efficiency. In addition, the crystallinity, perovskite composition, and film morphology are strongly dependent on the choice of the substrate (e.g. FTO, TiO$_2$, SiO$_2$/Si, etc.), which is expected to become critical when designing tandem cell architecture: the optimized evaporation conditions may differ according to the substrate on which OHP films are being deposited. With regard to vacuum systems that are usually needed for vapor based processing, special care is required for pumps (especially turbo molecular pumps).

For commercialization to take off, large area modules will be required.[190,191] A few attempts were made on large area (1 cm^2) fabrication based on vacuum- and CVD processes, Table 1, showing a promising PCE as high as 13.84%.[92] Because uniform, high-quality, and full-coverage OHP films are achievable, vacuum- and CVD processes are expected to have unique advantages in the fabrication of large-area OHP solar modules.[190]

The OHP materials are hygroscopic in nature, and are susceptible to degradation upon the intake of moisture.[192] Therefore, for protecting the core material in the OHP-based solar cells it requires stringent encapsulation. In addition to extrinsic degradation factors by moisture, the intrinsic stability of perovskites remains a major issue. The chemical reactions between moisture and perovskite need be carefully studied to
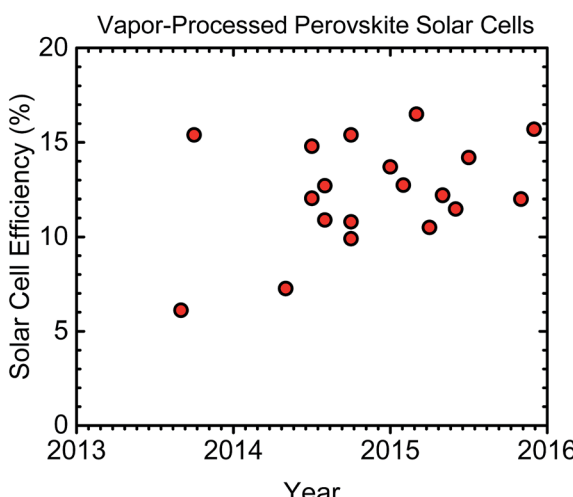
Fig. 12 Progress of solar cell efficiency in vapor-processed perovskite solar cells. The graph was generated based on the reported efficiencies shown in Table 1. A trend of increase in the number of published works on vapor-processed perovskites is inferred from the graph.

6708 | J. Mater. Chem. A, 2016, 4, 6693–6713

This journal is © The Royal Society of Chemistry 2016

unravel the reaction pathways, which provide insight for the development of methods (*e.g.* chemical composition engineering[2,153,193]) for stabilizing perovskites. The negative standard Gibbs free energy for iodide perovskite degradation was also reported in the absence of moisture.[161,192,194] The majority of stability tests reported in the literature, provides the lifetime profiles of OHP solar cells under the storage conditions (in N_2 or in ambient air). Only limited data exist for stability profiles under real operating conditions for vacuum- or CVD processed OHP solar cells.[109]

A major drawback of high efficient OHP solar cells is the use of Pb^{2+}, the material toxicity of which has been emphasized.[184,190,195] Efforts have been made to find alternatives such as Sn^{2+}. However, the instability of Sn^{2+} to form Sn^{4+} leads to a metal-like behavior and lowers the photovoltaic performance.[196] Many other elements in the periodic table (*e.g.* Co^{2+}, Fe^{2+}, Mn^{2+}, Pd^{2+}, and Ge^{2+}) were suggested as alternatives for Pb^{2+}.[24,163] Through comparison with the amount of lead used in lead acid batteries, a much lesser amount of lead is estimated to be required to produce 1000 GW per year from $CH_3NH_3PbI_3$ perovskite solar cells.[197] Therefore, tracking and minimizing the amounts of lead salt as well as quantifying solar cell efficiency normalized by the perovskite amount (*e.g.* PCE/thickness parameter calculated in Table 1) are proposed as important parameters to evaluate the toxicity at the times of disposal, recycling, and of eventual accidents.[184,190,195]

Acknowledgements

Notes and references

1 A. T. Barrows, A. J. Pearson, C. K. Kwak, A. D. F. Dunbar, A. R. Buckley and D. G. Lidzey, *Energy Environ. Sci.*, 2014, **7**, 2944–2950.

2 A. Mei, X. Li, L. Liu, Z. Ku, T. Liu, Y. Rong, M. Xu, M. Hu, J. Chen, Y. Yang, M. Grätzel and H. Han, *Science*, 2014, **345**, 295–298.

3 K. Hwang, Y.-S. Jung, Y.-J. Heo, F. H. Scholes, S. E. Watkins, J. Subbiah, D. J. Jones, D.-Y. Kim and D. Vak, *Adv. Mater.*, 2015, **27**, 1241–1247.

4 M. Z. Liu, M. B. Johnston and H. J. Snaith, *Nature*, 2013, **501**, 395–398.

5 O. Malinkiewicz, A. Yella, Y. H. Lee, G. M. Espallargas, M. Graetzel, M. K. Nazeeruddin and H. J. Bolink, *Nat. Photonics*, 2014, **8**, 128–132.

6 National Renewable Energy Laboratory (NREL), http://www.nrel.gov/ncpv/images/efficiency_chart.jpg.

7 W. S. Yang, J. H. Noh, N. J. Jeon, Y. C. Kim, S. Ryu, J. Seo and S. I. Seok, *Science*, 2015, **348**, 1234–1237.

8 Z. Fan, K. Sun and J. Wang, *J. Mater. Chem. A*, 2015, **3**, 18809–18828.

9 Q. Chen, N. de Marco, Y. Yang, T. B. Song, C. C. Chen, H. X. Zhao, Z. R. Hong, H. P. Zhou and Y. Yang, *Nano Today*, 2015, **10**, 355–396.

10 T. B. Song, Q. Chen, H. P. Zhou, C. Y. Jiang, H. H. Wang, Y. Yang, Y. S. Liu, J. B. You and Y. Yang, *J. Mater. Chem. A*, 2015, **3**, 9032–9050.

11 S. Kazim, M. K. Nazeeruddin, M. Grätzel and S. Ahmad, *Angew. Chem., Int. Ed.*, 2014, **53**, 2812–2824.

12 J. Berry, T. Buonassisi, D. A. Egger, G. Hodes, L. Kronik, Y.-L. Loo, I. Lubomirsky, S. R. Marder, Y. Mastai, J. S. Miller, D. B. Mitzi, Y. Paz, A. M. Rappe, I. Riess, B. Rybtchinski, O. Stafsudd, V. Stevanovic, M. F. Toney, D. Zitoun, A. Kahn, D. Ginley and D. Cahen, *Adv. Mater.*, 2015, **27**, 5102–5112.

13 N. G. Park, *J. Phys. Chem. Lett.*, 2013, **4**, 2423–2429.

14 H. J. Snaith, *J. Phys. Chem. Lett.*, 2013, **4**, 3623–3630.

15 M. A. Green, A. Ho-Baillie and H. J. Snaith, *Nat. Photonics*, 2014, **8**, 506–514.

16 N. G. Park, *Mater. Today*, 2015, **18**, 65–72.

17 P. Gao, M. Grätzel and M. K. Nazeeruddin, *Energy Environ. Sci.*, 2014, **7**, 2448–2463.

18 S. Q. Luo and W. A. Daoud, *J. Mater. Chem. A*, 2015, **3**, 8992–9010.

19 Y. Rong, L. Liu, A. Mei, X. Li and H. Han, *Adv. Energy Mater.*, 2015, **5**, 1501066.

20 H. Kim, K.-G. Lim and T.-W. Lee, *Energy Environ. Sci.*, 2015, DOI: 10.1039/c5ee02194d.

21 G. Giorgi, J.-I. Fujisawa, H. Segawa and K. Yamashita, *J. Phys. Chem. Lett.*, 2013, **4**, 4213–4216.

22 G. E. Eperon, G. M. Paterno, R. J. Sutton, A. Zampetti, A. A. Haghighirad, F. Cacialli and H. J. Snaith, *J. Mater. Chem. A*, 2015, **3**, 19688–19695.

23 G. E. Eperon, S. D. Stranks, C. Menelaou, M. B. Johnston, L. M. Herz and H. J. Snaith, *Energy Environ. Sci.*, 2014, **7**, 982–988.

24 M. R. Filip, G. E. Eperon, H. J. Snaith and F. Giustino, *Nat. Commun.*, 2014, **5**, 5757.

25 M. Grätzel, *Nat. Mater.*, 2014, **13**, 838–842.

26 H. Yu, F. Wang, F. Xie, W. Li, J. Chen and N. Zhao, *Adv. Funct. Mater.*, 2014, **24**, 7102–7108.

27 C. Wehrenfennig, M. Z. Liu, H. J. Snaith, M. B. Johnston and L. M. Herz, *Energy Environ. Sci.*, 2014, **7**, 2269–2275.

28 W.-J. Yin, T. Shi and Y. Yan, *Adv. Mater.*, 2014, **26**, 4653–4658.

29 W. J. Yin, J. H. Yang, J. Kang, Y. F. Yan and S. H. Wei, *J. Mater. Chem. A*, 2015, **3**, 8926–8942.

30 J. Kim, S. H. Lee, J. H. Lee and K. H. Hong, *J. Phys. Chem. Lett.*, 2014, **5**, 1312–1317.

31 W.-J. Yin, T. Shi and Y. Yan, *Appl. Phys. Lett.*, 2014, **104**, 063903.

32 D. Li, C. Liang, H. Zhang, C. Zhang, F. You and Z. He, *J. Appl. Phys.*, 2015, **117**, 074901.

33 C. Wehrenfennig, M. Z. Liu, H. J. Snaith, M. B. Johnston and L. M. Herz, *J. Phys. Chem. Lett.*, 2014, **5**, 1300–1306.

34 D. W. deQuilettes, S. M. Vorpahl, S. D. Stranks, H. Nagaoka, G. E. Eperon, M. E. Ziffer, H. J. Snaith and D. S. Ginger, *Science*, 2015, **348**, 683–686.

This journal is © The Royal Society of Chemistry 2016

J. Mater. Chem. A, 2016, **4**, 6693–6713 | 6709

35 V. D'Innocenzo, G. Grancini, M. J. Alcocer, A. R. Kandada, S. D. Stranks, M. M. Lee, G. Lanzani, H. J. Snaith and A. Petrozza, *Nat. Commun.*, 2014, **5**, 3586.

36 A. Marchioro, J. Teuscher, D. Friedrich, M. Kunst, R. van de Krol, T. Moehl, M. Grätzel and J. E. Moser, *Nat. Photonics*, 2014, **8**, 250–255.

37 Q. Lin, A. Armin, R. C. R. Nagiri, P. L. Burn and P. Meredith, *Nat. Photonics*, 2015, **9**, 106–112.

38 M. Hirasawa, T. Ishihara, T. Goto, K. Uchida and N. Miura, *Phys. B*, 1994, **201**, 427–430.

39 J. M. Frost, K. T. Butler, F. Brivio, C. H. Hendon, M. van Schilfgaarde and A. Walsh, *Nano Lett.*, 2014, **14**, 2584–2590.

40 C. R. Kagan, D. B. Mitzi and C. D. Dimitrakopoulos, *Science*, 1999, **286**, 945–947.

41 D. B. Mitzi, *Chem. Mater.*, 2001, **13**, 3283–3298.

42 D. B. Mitzi, K. Chondroudis and C. R. Kagan, *IBM J. Res. Dev.*, 2001, **45**, 29–45.

43 B. O'Regan and M. Grätzel, *Nature*, 1991, **353**, 737–740.

44 U. Bach, D. Lupo, P. Comte, J. E. Moser, F. Weissortel, J. Salbeck, H. Spreitzer and M. Grätzel, *Nature*, 1998, **395**, 583–585.

45 A. Kojima, K. Teshima, Y. Shirai and T. Miyasaka, *J. Am. Chem. Soc.*, 2009, **131**, 6050–6051.

46 H. S. Kim, C. R. Lee, J. H. Im, K. B. Lee, T. Moehl, A. Marchioro, S. J. Moon, R. Humphry-Baker, J. H. Yum, J. E. Moser, M. Grätzel and N. G. Park, *Sci. Rep.*, 2012, **2**, 591.

47 M. M. Lee, J. Teuscher, T. Miyasaka, T. N. Murakami and H. J. Snaith, *Science*, 2012, **338**, 643–647.

48 H. S. Kim, S. H. Im and N. G. Park, *J. Phys. Chem. C*, 2014, **118**, 5615–5625.

49 S. Kazim, M. K. Nazeeruddin, M. Grätzel and S. Ahmad, *Angew. Chem., Int. Ed.*, 2014, **53**, 2812–2824.

50 H. Zhou, Q. Chen, G. Li, S. Luo, T.-b. Song, H.-S. Duan, Z. Hong, J. You, Y. Liu and Y. Yang, *Science*, 2014, **345**, 542–546.

51 L. Etgar, P. Gao, Z. Xue, Q. Peng, A. K. Chandiran, B. Liu, M. K. Nazeeruddin and M. Grätzel, *J. Am. Chem. Soc.*, 2012, **134**, 17396–17399.

52 E. J. Juarez-Perez, M. Wußler, F. Fabregat-Santiago, K. Lakus-Wollny, E. Mankel, T. Mayer, W. Jaegermann and I. Mora-Sero, *J. Phys. Chem. Lett.*, 2014, **5**, 680–685.

53 K. Wojciechowski, M. Saliba, T. Leijtens, A. Abate and H. J. Snaith, *Energy Environ. Sci.*, 2014, **7**, 1142–1147.

54 B. Conings, L. Baeten, C. De Dobbelaere, J. D'Haen, J. Manca and H. G. Boyen, *Adv. Mater.*, 2014, **26**, 2041–2046.

55 B. Cai, Y. Xing, Z. Yang, W.-H. Zhang and J. Qiu, *Energy Environ. Sci.*, 2013, **6**, 1480–1485.

56 E. Edri, S. Kirmayer, D. Cahen and G. Hodes, *J. Phys. Chem. Lett.*, 2013, **4**, 897–902.

57 J. T. W. Wang, J. M. Ball, E. M. Barea, A. Abate, J. A. Alexander-Webber, J. Huang, M. Saliba, I. Mora-Sero, J. Bisquert, H. J. Snaith and R. J. Nicholas, *Nano Lett.*, 2014, **14**, 724–730.

58 K. N. Liang, D. B. Mitzi and M. T. Prikas, *Chem. Mater.*, 1998, **10**, 403–411.

59 J. Burschka, N. Pellet, S. J. Moon, R. Humphry-Baker, P. Gao, M. K. Nazeeruddin and M. Grätzel, *Nature*, 2013, **499**, 316–319.

60 D. Q. Bi, S. J. Moon, L. Haggman, G. Boschloo, L. Yang, E. M. J. Johansson, M. K. Nazeeruddin, M. Grätzel and A. Hagfeldt, *RSC Adv.*, 2013, **3**, 18762–18766.

61 Y. Y. Zhou, M. J. Yang, W. W. Wu, A. L. Vasiliev, K. Zhu and N. P. Padture, *J. Mater. Chem. A*, 2015, **3**, 8178–8184.

62 Q. Chen, H. Zhou, Z. Hong, S. Luo, H.-S. Duan, H.-H. Wang, Y. Liu, G. Li and Y. Yang, *J. Am. Chem. Soc.*, 2013, **136**, 622–625.

63 Q. Chen, H. Zhou, T.-B. Song, S. Luo, Z. Hong, H.-S. Duan, L. Dou, Y. Liu and Y. Yang, *Nano Lett.*, 2014, **14**, 4158–4163.

64 C. Ying, C. W. Shi, N. Wu, J. C. Zhang and M. Wang, *Nanoscale*, 2015, **7**, 12092–12095.

65 H. Zhou, Q. Chen and Y. Yang, *MRS Bull.*, 2015, **40**, 667–673.

66 G. Balaji, P. H. Joshi, H. A. Abbas, L. Zhang, R. Kottokkaran, M. Samiee, M. Noack and V. L. Dalal, *Phys. Chem. Chem. Phys.*, 2015, **17**, 10369–10372.

67 R. Sheng, A. Ho-Baillie, S. J. Huang, S. Chen, X. M. Wen, X. J. Hao and M. A. Green, *J. Phys. Chem. C*, 2015, **119**, 3545–3549.

68 Y. B. Li, J. K. Cooper, R. Buonsanti, C. Giannini, Y. Liu, F. M. Toma and I. D. Sharp, *J. Phys. Chem. Lett.*, 2015, **6**, 493–499.

69 T. Du, N. Wang, H. Chen, H. Lin and H. He, *ACS Appl. Mater. Interfaces*, 2015, **7**, 3382–3388.

70 C. Momblona, O. Malinkiewicz, C. Roldán-Carmona, A. Soriano, L. Gil-Escrig, E. Bandiello, M. Scheepers, E. Edri and H. J. Bolink, *APL Mater.*, 2014, **2**, 081504.

71 O. Malinkiewicz, C. Roldán-Carmona, A. Soriano, E. Bandiello, L. Camacho, M. K. Nazeeruddin and H. J. Bolink, *Adv. Energy Mater.*, 2014, **4**, 1400345.

72 A. S. Subbiah, A. Halder, S. Ghosh, N. Mahuli, G. Hodes and S. K. Sarkar, *J. Phys. Chem. Lett.*, 2014, **5**, 1748–1753.

73 B. S. Kim, T. M. Kim, M. S. Choi, H. S. Shim and J. J. Kim, *Org. Electron.*, 2015, **17**, 102–106.

74 L. E. Polander, P. Pahner, M. Schwarze, M. Saalfrank, C. Koerner and K. Leo, *APL Mater.*, 2014, **2**, 081503.

75 M. Sessolo, C. Momblona, L. Gil-Escrig and H. J. Bolink, *MRS Bull.*, 2015, **40**, 660–666.

76 T.-W. Ng, C.-Y. Chan, M.-F. Lo, Z. Q. Guan and C.-S. Lee, *J. Mater. Chem. A*, 2015, **3**, 9081–9085.

77 C. Gao, J. Liu, C. Liao, Q. Y. Ye, Y. Z. Zhang, X. L. He, X. W. Guo, J. Mei and W. M. Lau, *RSC Adv.*, 2015, **5**, 26175–26180.

78 L. K. Ono, S. Wang, Y. Kato, S. R. Raga and Y. B. Qi, *Energy Environ. Sci.*, 2014, **7**, 3989–3993.

79 S. Wang, L. K. Ono, M. R. Leyden, Y. Kato, S. R. Raga, M. V. Lee and Y. B. Qi, *J. Mater. Chem. A*, 2015, **3**, 14631–14641.

80 J. Teuscher, A. Ulianov, O. Müntener, M. Grätzel and N. Tétreault, *ChemSusChem*, 2015, **8**, 3847–3852.

81 D. Zhao, W. Ke, C. R. Grice, A. J. Cimaroli, X. Tan, M. Yang, R. W. Collins, H. Zhang, K. Zhu and Y. Yan, *Nano Energy*, 2015, **19**, 88–97.

6710 | *J. Mater. Chem. A*, 2016, **4**, 6693–6713

This journal is © The Royal Society of Chemistry 2016

82 M. R. Leyden, L. K. Ono, S. R. Raga, Y. Kato, S. H. Wang and Y. B. Qi, *J. Mater. Chem. A*, 2014, **2**, 18742–18745.

83 M. R. Leyden, M. V. Lee, S. R. Raga and Y. B. Qi, *J. Mater. Chem. A*, 2015, **3**, 16097–16103.

84 P. F. Luo, Z. F. Liu, W. Xia, C. C. Yuan, J. G. Cheng and Y. W. Lu, *J. Mater. Chem. A*, 2015, **3**, 12443–12451.

85 P. F. Luo, Z. F. Liu, W. Xia, C. C. Yuan, J. G. Cheng and Y. W. Lu, *ACS Appl. Mater. Interfaces*, 2015, **7**, 2708–2714.

86 P. Luo, Z. Liu, W. Xia, C. Yuan, J. Cheng, C. Xu and Y. Lu, *J. Mater. Chem. A*, 2015, **3**, 22949–22959.

87 Y. Peng, G. Jing and T. Cui, *RSC Adv.*, 2015, **5**, 95847–95853.

88 C.-W. Chen, H.-W. Kang, S.-Y. Hsiao, P.-F. Yang, K.-M. Chiang and H.-W. Lin, *Adv. Mater.*, 2014, **26**, 6647–6652.

89 H. Hu, D. Wang, Y. Y. Zhou, J. L. Zhang, S. L. Lv, S. P. Pang, X. Chen, Z. H. Liu, N. P. Padture and G. L. Cui, *RSC Adv.*, 2014, **4**, 28964–28967.

90 A. Ng, Z. Ren, Q. Shen, S. H. Cheung, H. C. Gokkaya, G. Bai, J. Wang, L. Yang, S. K. So, A. B. Djurisic, W. W.-f. Leung, J. Hao, W. K. Chan and C. Surya, *J. Mater. Chem. A*, 2015, **3**, 9223–9231.

91 H. A. Abbas, R. Kottokkaran, B. Ganapathy, M. Samiee, L. Zhang, A. Kitahara, M. Noack and V. L. Dalal, *APL Mater.*, 2015, **3**, 016105.

92 D. Yang, Z. Yang, W. Qin, Y. L. Zhang, S. Z. Liu and C. Li, *J. Mater. Chem. A*, 2015, **3**, 9401–9405.

93 G. Longo, L. Gil-Escrig, M. J. Degen, M. Sessolo and H. J. Bolink, *Chem. Commun.*, 2015, **51**, 7376–7378.

94 A. Dualeh, N. Tétreault, T. Moehl, P. Gao, M. K. Nazeeruddin and M. Grätzel, *Adv. Funct. Mater.*, 2014, **24**, 3250–3258.

95 G. E. Eperon, V. M. Burlakov, P. Docampo, A. Goriely and H. J. Snaith, *Adv. Funct. Mater.*, 2014, **24**, 151–157.

96 P.-W. Liang, C.-Y. Liao, C.-C. Chueh, F. Zuo, S. T. Williams, X.-K. Xin, J. Lin and A. K. Y. Jen, *Adv. Mater.*, 2014, **26**, 3748–3754.

97 D. B. Mitzi, M. T. Prikas and K. Chondroudis, *Chem. Mater.*, 1999, **11**, 542–544.

98 N. J. Jeon, J. H. Noh, W. S. Yang, Y. C. Kim, S. Ryu, J. Seo and S. I. Seok, *Nature*, 2015, **517**, 476–480.

99 D. T. Moore, H. Sai, K. W. Tan, D.-M. Smilgies, W. Zhang, H. J. Snaith, U. Wiesner and L. A. Estroff, *J. Am. Chem. Soc.*, 2015, **137**, 2350–2358.

100 M. Toshinori, F. Katsuhiko and T. Tetsuo, *Jpn. J. Appl. Phys.*, 2006, **45**, 523.

101 F. Hao, C. C. Stoumpos, Z. Liu, R. P. H. Chang and M. G. Kanatzidis, *J. Am. Chem. Soc.*, 2014, **136**, 16411–16419.

102 J. B. You, Y. M. Yang, Z. R. Hong, T. B. Song, L. Meng, Y. S. Liu, C. Y. Jiang, H. P. Zhou, W. H. Chang, G. Li and Y. Yang, *Appl. Phys. Lett.*, 2014, **105**, 183902.

103 N. J. Jeon, J. H. Noh, Y. C. Kim, W. S. Yang, S. Ryu and S. I. Seok, *Nat. Mater.*, 2014, **13**, 897–903.

104 M. Era, T. Hattori, T. Taira and T. Tsutsui, *Chem. Mater.*, 1997, **9**, 8–10.

105 A. M. Salau, *Sol. Energy Mater.*, 1980, **2**, 327–332.

106 L. K. Ono, P. Schulz, J. J. Endres, G. O. Nikiforov, Y. Kato, A. Kahn and Y. B. Qi, *J. Phys. Chem. Lett.*, 2014, **5**, 1374–1379.

107 Z. Hawash, L. K. Ono, S. R. Raga, M. V. Lee and Y. B. Qi, *Chem. Mater.*, 2015, **27**, 562–569.

108 M. C. Jung, S. R. Raga, L. K. Ono and Y. B. Qi, *Sci. Rep.*, 2015, **5**, 9863.

109 L. K. Ono, S. R. Raga, M. Remeika, A. J. Winchester, A. Gabe and Y. B. Qi, *J. Mater. Chem. A*, 2015, **3**, 15451–15456.

110 J. A. Christians, R. C. M. Fung and P. V. Kamat, *J. Am. Chem. Soc.*, 2014, **136**, 758–764.

111 S. Ito, S. Tanaka, H. Vahlman, H. Nishino, K. Manabe and P. Lund, *ChemPhysChem*, 2014, **15**, 1194–1200.

112 P. Schulz, E. Edri, S. Kirmayer, G. Hodes, D. Cahen and A. Kahn, *Energy Environ. Sci.*, 2014, **7**, 1377–1381.

113 R. F. Service, *Science*, 2014, **344**, 458.

114 G. E. Eperon, V. M. Burlakov, A. Goriely and H. J. Snaith, *ACS Nano*, 2014, **8**, 591–598.

115 Y. Zhao and K. Zhu, *J. Phys. Chem. C*, 2014, **118**, 9412–9418.

116 R. S. Sanchez, V. Gonzalez-Pedro, J.-W. Lee, N.-G. Park, Y. S. Kang, I. Mora-Sero and J. Bisquert, *J. Phys. Chem. Lett.*, 2014, **5**, 2357–2363.

117 V. Gonzalez-Pedro, E. J. Juarez-Perez, W.-S. Arsyad, E. M. Barea, F. Fabregat-Santiago, I. Mora-Sero and J. Bisquert, *Nano Lett.*, 2014, **14**, 888–893.

118 B. Wang and T. Chen, *Adv. Sci.*, 2015, DOI: 10.1002/advs.201500262.

119 Y. K. Peng, G. S. Jing and T. H. Cui, *J. Mater. Chem. A*, 2015, **3**, 12436–12442.

120 S. T. Ha, X. Liu, Q. Zhang, D. Giovanni, T. C. Sum and Q. Xiong, *Adv. Opt. Mater.*, 2014, **2**, 838–844.

121 Q. Zhang, S. T. Ha, X. Liu, T. C. Sum and Q. Xiong, *Nano Lett.*, 2014, **14**, 5995–6001.

122 J. Xing, X. F. Liu, Q. Zhang, S. T. Ha, Y. W. Yuan, C. Shen, T. C. Sum and Q. Xiong, *Nano Lett.*, 2015, **15**, 4571–4577.

123 D. J. Lewis and P. O'Brien, *Chem. Commun.*, 2014, **50**, 6319–6321.

124 D. S. Bhachu, D. O. Scanlon, E. J. Saban, H. Bronstein, I. P. Parkin, C. J. Carmalt and R. G. Palgrave, *J. Mater. Chem. A*, 2015, **3**, 9071–9073.

125 M. M. Tavakoli, L. Gu, Y. Gao, C. Reckmeier, J. He, A. L. Rogach, Y. Yao and Z. Fan, *Sci. Rep.*, 2015, **5**, 14083.

126 M. Era, K. Maeda and T. Tsutsui, *Thin Solid Films*, 1998, **331**, 285–290.

127 Z. Ren, A. Ng, Q. Shen, H. C. Gokkaya, J. Wang, L. Yang, W.-K. Yiu, G. Bai, A. B. Djurišić, W. W.-f. Leung, J. Hao, W. K. Chan and C. Surya, *Sci. Rep.*, 2014, **4**, 6752.

128 B. R. Sutherland, S. Hoogland, M. M. Adachi, P. Kanjanaboos, C. T. O. Wong, J. J. McDowell, J. X. Xu, O. Voznyy, Z. J. Ning, A. J. Houtepen and E. H. Sargent, *Adv. Mater.*, 2015, **27**, 53–58.

129 B. R. Sutherland, S. Hoogland, M. M. Adachi, C. T. O. Wong and E. H. Sargent, *ACS Nano*, 2014, **8**, 10947–10952.

130 L. Harris and B. M. Siegel, *J. Appl. Phys.*, 1948, **19**, 739–741.

131 J. L. Richards, P. B. Hart and L. M. Gallone, *J. Appl. Phys.*, 1963, **34**, 3418–3420.

This journal is © The Royal Society of Chemistry 2016

J. Mater. Chem. A, 2016, **4**, 6693–6713 | 6711

132 E. K. Müller, B. J. Nicholson and G. L. E. Turner, *J. Electrochem. Soc.*, 1963, **110**, 969–973.

133 K. Chondroudis, D. B. Mitzi and P. Brock, *Chem. Mater.*, 2000, **12**, 169–175.

134 F. Chiarella, A. Zappettini, F. Licci, I. Borriello, G. Cantele, D. Ninno, A. Cassinese and R. Vaglio, *Phys. Rev. B: Condens. Matter Mater. Phys.*, 2008, **77**, 045129.

135 S. Ahmad, C. Hanmandlu, P. K. Kanaujia and G. V. Prakash, *Opt. Mater. Express*, 2014, **4**, 1313–1323.

136 G.-X. Liang, P. Fan, J.-T. Luo, D. Gu and Z.-H. Zheng, *Prog. Photovolt: Res. Appl.*, 2015, **23**, 1901–1907.

137 S. R. Raga, M.-C. Jung, M. V. Lee, M. R. Leyden, Y. Kato and Y. B. Qi, *Chem. Mater.*, 2015, **27**, 1597–1603.

138 T. Miyadera, Y. Shibata, T. Koganezawa, T. N. Murakami, T. Sugita, N. Tanigaki and M. Chikamatsu, *Nano Lett.*, 2015, **15**, 5630–5634.

139 C. G. Wang, X. L. Liu, C. C. Wang, Z. G. Xiao, C. Bi, Y. C. Shao, J. S. Huang and Y. L. Gao, *J. Vac. Sci. Technol., B*, 2015, **33**, 032401.

140 A. Calloni, A. Abate, G. Bussetti, G. Berti, R. Yivlialin, F. Ciccacci and L. Duò, *J. Phys. Chem. C*, 2015, **119**, 21329–21335.

141 R. Lindblad, D. Bi, B.-w. Park, J. Oscarsson, M. Gorgoi, H. Siegbahn, M. Odelius, E. M. J. Johansson and H. Rensmo, *J. Phys. Chem. Lett.*, 2014, **5**, 648–653.

142 Q. K. Wang, R. B. Wang, P. F. Shen, C. Li, Y. Q. Li, L. J. Liu, S. Duhm and J. X. Tang, *Adv. Mater. Interfaces*, 2015, **2**, 1400528.

143 L. A. Frolova, N. N. Dremova and P. A. Troshin, *Chem. Commun.*, 2015, **51**, 14917–14920.

144 P. Liu, X. L. Liu, L. Lyu, H. P. Xie, H. Zhang, D. M. Niu, H. Huang, C. Bi, Z. G. Xiao, J. S. Huang and Y. L. Gao, *Appl. Phys. Lett.*, 2015, **106**, 193903.

145 X. L. Liu, C. G. Wang, L. Lyu, C. C. Wang, Z. G. Xiao, C. Bi, J. S. Huang and Y. L. Gao, *Phys. Chem. Chem. Phys.*, 2015, **17**, 896–902.

146 E. M. Miller, Y. X. Zhao, C. C. Mercado, S. K. Saha, J. M. Luther, K. Zhu, V. Stevanovic, C. L. Perkins and J. van de Lagemaat, *Phys. Chem. Chem. Phys.*, 2014, **16**, 22122–22130.

147 S. Chen, T. W. Goh, D. Sabba, J. Chua, N. Mathews, C. H. A. Huan and T. C. Sum, *APL Mater.*, 2014, **2**, 081512.

148 Q. Wang, Y. Shao, H. Xie, L. Lyu, X. Liu, Y. Gao and J. Huang, *Appl. Phys. Lett.*, 2014, **105**, 163508.

149 B. J. Foley, D. L. Marlowe, K. Y. Sun, W. A. Saidi, L. Scudiero, M. C. Gupta and J. J. Choi, *Appl. Phys. Lett.*, 2015, **106**, 243904.

150 I. Deretzis, A. Alberti, G. Pellegrino, E. Smecca, F. Giannazzo, N. Sakai, T. Miyasaka and A. La Magna, *Appl. Phys. Lett.*, 2015, **106**, 131904.

151 P. Pistor, J. Borchert, W. Fränzel, R. Csuk and R. Scheer, *J. Phys. Chem. Lett.*, 2014, **5**, 3308–3312.

152 J. Borchert, H. Boht, W. Franzel, R. Csuk, R. Scheer and P. Pistor, *J. Mater. Chem. A*, 2015, **3**, 19842–19849.

153 J. H. Noh, S. H. Im, J. H. Heo, T. N. Mandal and S. I. Seok, *Nano Lett.*, 2013, **13**, 1764–1769.

154 E. Mosconi, A. Amat, M. K. Nazeeruddin, M. Grätzel and F. de Angelis, *J. Phys. Chem. C*, 2013, **117**, 13902–13913.

155 S. Colella, E. Mosconi, P. Fedeli, A. Listorti, F. Gazza, F. Orlandi, P. Ferro, T. Besagni, A. Rizzo, G. Calestani, G. Gigli, F. de Angelis and R. Mosca, *Chem. Mater.*, 2013, **25**, 4613–4618.

156 M. I. Dar, N. Arora, P. Gao, S. Ahmad, M. Grätzel and M. K. Nazeeruddin, *Nano Lett.*, 2014, **14**, 6991–6996.

157 L. Liu, J. A. McLeod, R. Wang, P. Shen and S. Duhm, *Appl. Phys. Lett.*, 2015, **107**, 061904.

158 T. W. Ng, C. Y. Chan, Q. D. Yang, H. X. Wei, M. F. Lo, V. A. L. Roy, W. J. Zhang and C. S. Lee, *Org. Electron.*, 2013, **14**, 2743–2747.

159 Y. Li, X. Xu, C. Wang, C. Wang, F. Xie, J. Yang and Y. Gao, *AIP Adv.*, 2015, **5**, 097111.

160 Y. Li, X. Xu, C. Wang, C. Wang, F. Xie, J. Yang and Y. Gao, *J. Phys. Chem. C*, 2015, **119**, 23996–24002.

161 G. D. Niu, X. D. Guo and L. D. Wang, *J. Mater. Chem. A*, 2015, **3**, 8970–8980.

162 T. Leijtens, G. E. Eperon, N. K. Noel, S. N. Habisreutinger, A. Petrozza and H. J. Snaith, *Adv. Energy Mater.*, 2015, **5**, 1500963.

163 P. P. Boix, K. Nonomura, N. Mathews and S. G. Mhaisalkar, *Mater. Today*, 2014, **17**, 16–23.

164 D. Cahen, A. Kahn and E. Umbach, *Mater. Today*, 2005, **8**, 32–41.

165 H. J. Snaith, A. Abate, J. M. Ball, G. E. Eperon, T. Leijtens, N. K. Noel, S. D. Stranks, J. T.-W. Wang, K. Wojciechowski and W. Zhang, *J. Phys. Chem. Lett.*, 2014, **5**, 1511–1515.

166 H.-S. Kim and N.-G. Park, *J. Phys. Chem. Lett.*, 2014, **5**, 2927–2934.

167 E. L. Unger, E. T. Hoke, C. D. Bailie, W. H. Nguyen, A. R. Bowring, T. Heumuller, M. G. Christoforo and M. D. McGehee, *Energy Environ. Sci.*, 2014, **7**, 3690–3698.

168 L. K. Ono, S. R. Raga, S. Wang, Y. Kato and Y. B. Qi, *J. Mater. Chem. A*, 2015, **3**, 9074–9080.

169 W. Tress, N. Marinova, T. Moehl, S. M. Zakeeruddin, M. K. Nazeeruddin and M. Grätzel, *Energy Environ. Sci.*, 2015, **8**, 995–1004.

170 B. Wu, K. Fu, N. Yantara, G. Xing, S. Sun, T. C. Sum and N. Mathews, *Adv. Energy Mater.*, 2015, **5**, 1500829.

171 Z. Xiao, Y. Yuan, Y. Shao, Q. Wang, Q. Dong, C. Bi, P. Sharma, A. Gruverman and J. Huang, *Nat. Mater.*, 2015, **14**, 193–198.

172 Y. Zhao, C. J. Liang, H. M. Zhang, D. Li, D. Tian, G. B. Li, X. P. Jing, W. G. Zhang, W. K. Xiao, Q. Liu, F. J. Zhang and Z. Q. He, *Energy Environ. Sci.*, 2015, **8**, 1256–1260.

173 Y. Zhang, M. Liu, G. E. Eperon, T. C. Leijtens, D. McMeekin, M. Saliba, W. Zhang, M. de Bastiani, A. Petrozza, L. M. Herz, M. B. Johnston, H. Lin and H. J. Snaith, *Mater. Horiz.*, 2015, **2**, 315–322.

174 J. M. Azpiroz, E. Mosconi, J. Bisquert and F. de Angelis, *Energy Environ. Sci.*, 2015, **8**, 2118–2127.

175 C. Zhao, B. Chen, X. Qiao, L. Luan, K. Lu and B. Hu, *Adv. Energy Mater.*, 2015, **5**, 1500279.

6712 | *J. Mater. Chem. A*, 2016, **4**, 6693–6713

This journal is © The Royal Society of Chemistry 2016

176 J. Beilsten-Edmands, G. E. Eperon, R. D. Johnson, H. J. Snaith and P. G. Radaelli, *Appl. Phys. Lett.*, 2015, **106**, 173502.

177 A. Dualeh, T. Moehl, N. Tétreault, J. Teuscher, P. Gao, M. K. Nazeeruddin and M. Grätzel, *ACS Nano*, 2014, **8**, 362–373.

178 M. Kaltenbrunner, G. Adam, E. D. Glowacki, M. Drack, R. Schwodiauer, L. Leonat, D. H. Apaydin, H. Groiss, M. C. Scharber, M. S. White, N. S. Sariciftci and S. Bauer, *Nat. Mater.*, 2015, **14**, 1032.

179 J. S. Luo, J. H. Im, M. T. Mayer, M. Schreier, M. K. Nazeeruddin, N. G. Park, S. D. Tilley, H. J. Fan and M. Grätzel, *Science*, 2014, **345**, 1593–1596.

180 J. T. Xu, Y. H. Chen and L. M. Dai, *Nat. Commun.*, 2015, **6**, 8103.

181 Z. K. Tan, R. S. Moghaddam, M. L. Lai, P. Docampo, R. Higler, F. Deschler, M. Price, A. Sadhanala, L. M. Pazos, D. Credgington, F. Hanusch, T. Bein, H. J. Snaith and R. H. Friend, *Nat. Nanotechnol.*, 2014, **9**, 687–692.

182 H. Zhu, Y. Fu, F. Meng, X. Wu, Z. Gong, Q. Ding, M. V. Gustafsson, M. T. Trinh, S. Jin and X. Y. Zhu, *Nat. Mater.*, 2015, **14**, 636–642.

183 L. Dou, Y. Yang, J. You, Z. Hong, W.-H. Chang, G. Li and Y. Yang, *Nat. Commun.*, 2014, **5**, 5404.

184 N. Espinosa, L. Serrano-Lujan, A. Urbina and F. C. Krebs, *Sol. Energy Mater. Sol. Cells*, 2015, **137**, 303–310.

185 B. E. Hardin, H. J. Snaith and M. D. McGehee, *Nat. Photonics*, 2012, **6**, 162–169.

186 A. A. Asif, R. Singh and G. F. Alapatt, *J. Renewable Sustainable Energy*, 2015, **7**, 043120.

187 A. Fakharuddin, R. Jose, T. M. Brown, F. Fabregat-Santiago and J. Bisquert, *Energy Environ. Sci.*, 2014, **7**, 3952–3981.

188 W. Chen, Y. Wu, Y. Yue, J. Liu, W. Zhang, X. Yang, H. Chen, E. Bi, I. Ashraful, M. Grätzel and L. Han, *Science*, 2015, **350**, 944–948.

189 J. A. Christians, J. S. Manser and P. V. Kamat, *J. Phys. Chem. Lett.*, 2015, **6**, 852–857.

190 J. Gong, S. B. Darling and F. Q. You, *Energy Environ. Sci.*, 2015, **8**, 1953–1968.

191 S. Razza, F. Di Giacomo, F. Matteocci, L. Cinà, A. L. Palma, S. Casaluci, P. Cameron, A. D'Epifanio, S. Licoccia, A. Reale, T. M. Brown and A. Di Carlo, *J. Power Sources*, 2015, **277**, 286–291.

192 Y. Kato, L. K. Ono, M. V. Lee, S. H. Wang, S. R. Raga and Y. B. Qi, *Adv. Mater. Interfaces*, 2015, **2**, 1500195.

193 N. Pellet, P. Gao, G. Gregori, T.-Y. Yang, M. K. Nazeeruddin, J. Maier and M. Grätzel, *Angew. Chem., Int. Ed.*, 2014, **53**, 3151–3157.

194 A. Alberti, I. Deretzis, G. Pellegrino, C. Bongiorno, E. Smecca, G. Mannino, F. Giannazzo, G. G. Condorelli, N. Sakai, T. Miyasaka, C. Spinella and A. La Magna, *ChemPhysChem*, 2015, **16**, 3064–3071.

195 L. Serrano-Lujan, N. Espinosa, T. T. Larsen-Olsen, J. Abad, A. Urbina and F. C. Krebs, *Adv. Energy Mater.*, 2015, **5**, 1501119.

196 C. C. Stoumpos, C. D. Malliakas and M. G. Kanatzidis, *Inorg. Chem.*, 2013, **52**, 9019–9038.

197 G. Hodes, *Science*, 2013, **342**, 317–318.

This journal is © The Royal Society of Chemistry 2016

J. Mater. Chem. A, 2016, **4**, 6693–6713 | 6713